Atmos. Chem. Phys., 26, 2443–2463, 2026
https://doi.org/10.5194/acp-26-2443-2026

Atmospheric Chemistry and Physics
Open Access
EGU

Photochemical and ozone-induced aging significantly alter the viscosity of aqueous *trans*-aconitic acid aerosol particles

Cynthia Antossian[1], **Marcel Müller**[1,a], **and Ulrich K. Krieger**[1]

[1]Institute for Atmospheric and Climate Science, ETH Zurich, Universitätstrasse 16, 8092 Zurich, Switzerland
[a]currently at: Institute of Biogeochemistry and Pollutant Dynamics, ETH Zurich, Universitätstrasse 16, 8092 Zurich, Switzerland

Correspondence: Cynthia Antossian (cynthia.antossian@env.ethz.ch) and Ulrich K. Krieger (ulrich.krieger@env.ethz.ch)

Received: 28 November 2025 – Discussion started: 4 December 2025
Revised: 3 February 2026 – Accepted: 5 February 2026 – Published: 17 February 2026

Abstract. Aging processes of organic aerosols, including reactions with gas phase oxidants, such as ozone (O_3), as well as photochemical reactions, can significantly alter their physicochemical properties. While previous research has examined how photochemical aging and ozonolysis affect the physicochemical properties of organic aerosols, our study investigates the combined effect of photolysis and ozonolysis. We use aqueous *trans*-aconitic acid as a proxy for secondary organic aerosol particles (SOA), selected for its ability to absorb UV light and for containing a C=C double bond that is susceptible to ozonolysis. We observe significant mass loss in single particles levitated in an electrodynamic balance when exposed to either O_3 or UV light (375 nm), as well as to both aging processes simultaneously, resulting from fragmentation reactions followed by the volatilization of some of the products. Viscosity measurements at 17 % relative humidity revealed an increase of nearly 4 orders of magnitude after both UV exposure and combined UV and O_3 exposure at 60 % mass loss. Interestingly, continued UV-aging beyond 60 % mass loss resulted in a viscosity decrease, whereas combined UV and O_3 exposure led to a further viscosity increase. Hygroscopicity exhibited only a modest decline after 20 % mass loss during UV-aging and remained constant with further UV exposure; this reduction was less pronounced when UV-aging occurred in the presence of O_3. Overall, our results indicate that the mixing times within accumulation mode SOA particles may increase from 4 s to 4 h after aging under dry boundary layer conditions.

1 Introduction

Aerosol particles play a prominent role in the atmosphere, since they are involved in many important processes including cloud formation, biogeochemical cycling, and light scattering (Seinfeld and Pandis, 2016). Moreover, aerosols affect human health, since they have been associated with respiratory and cardiac diseases, oxidative stress, and cancer (Dockery and Pope, 1994; Nel, 2005). Organic compounds constitute a major fraction of atmospheric aerosols (20 %–90 %) (Kanakidou et al., 2005; Jimenez et al., 2009). A significant fraction of these aerosols are secondary organic aerosols (SOA) (Zhang et al., 2007), which are formed when volatile organic compounds oxidize and produce compounds with low volatility that partition from the gas phase into the particle phase, eventually forming SOA (Pankow, 1994). In addition, these low volatility compounds can partition into pre-existing aerosols, leading to internal mixing of primary and secondary aerosol particles (Marcolli et al., 2004; Marcolli and Krieger, 2020)

Throughout their lifetimes in the atmosphere, these organic aerosol particles undergo various aging processes. One of these processes are reactions with gas phase oxidants, such as ozone (O_3), hydroxyl radicals (OH), and nitrate radicals (NO_3). In addition to the reactions with oxidants, organic aerosols can undergo photochemical reactions due to expo-

sure to UV or even visible light, either directly or indirectly by photosensitizers, leading to additional aging. Oxidation reactions can occur through different pathways (Kroll and Seinfeld, 2008), depending on the chemical composition of the gas and particle phase and on the atmospheric conditions, such as temperature and relative humidity (RH). For instance, fragmentation can take place because of carbon-carbon double bond cleavage, leading to more volatile products that volatilize from the particle. Functionalization can also take place because of the addition of polar functional groups, thus increasing oxygen-to-carbon ratio O : C and forming more hygroscopic, higher molecular weight products that have low volatility. In addition, oligomerization or accretion can occur through the association of small molecules, consequently forming products with similar O : C, but higher number of carbon atoms that have low hygroscopicity, low volatility, and high viscosity (Kroll and Seinfeld, 2008). Fragmentation reactions have been observed for a range of organic aerosol particles during photochemical aging or when exposed to atmospheric oxidants (O'Brien and Kroll, 2019; Sun and Smith, 2024; Dou et al., 2021; Kroll et al., 2015). Moreover, oxidation of SOA has been shown to induce the formation of oligomers through accretion reactions e.g. Kalberer et al. (2004). At present, it remains uncertain which mechanisms dominate under different aerosol compositions and atmospheric conditions, making it challenging to predict aerosol properties during and after aging.

These aging processes can significantly alter the physicochemical properties of organic aerosols, such as the viscosity and hygroscopicity (Hosny et al., 2016; Athanasiadis et al., 2016; Baboomian et al., 2022; Jimenez et al., 2009; Kroll et al., 2011; Kroll et al., 2015). Viscosity of organic aerosols varies over a wide range, depending on the chemical properties, such as molecular structure, functional groups, chain length, molecular weight, and carbon oxidation state and on the environmental conditions, such as temperature and relative humidity (Gou et al., 2025). Moreover, the viscosity of organic aerosols is an indication of the phase state, with aerosols having viscosity values less than 10^2 Pa s considered as being liquid, between 10^2 and 10^{12} Pa s semi-solid, and greater than 10^{12} Pa s solid (Shiraiwa et al., 2011; Koop et al., 2011).

Viscosity affects the condensed phase chemistry (Pöschl and Shiraiwa, 2015; Kuwata and Martin, 2012), gas-particle partitioning (Shiraiwa et al., 2011; Zaveri et al., 2014), and the ability of the aerosol particle to act as ice nucleating particles (Wolf et al., 2020; Murray et al., 2010), while hygroscopicity affects the ability of the particle to act as cloud condensation nuclei (Chan et al., 2008), thereby affecting the Earth's energy budget and climate. Moreover, viscosity affects the ability of the particle to react with other chemical species. Viscous aerosols can limit molecular motion due to slow diffusion of oxidants, water, and organic compounds (Pöschl and Shiraiwa, 2015). This makes particulate air pollutants less susceptible to degradation and increases their mixing times in the troposphere, thereby favoring their transport and affecting human health (Mu et al., 2018; Bastelberger et al., 2017). For instance, polycyclic aromatic hydrocarbons (PAHs) that were coated with viscous organic aerosols, were shielded from oxidation, highlighting stronger long-range transport and elevated lung cancer risk (Shrivastava et al., 2017; Zelenyuk et al., 2012).

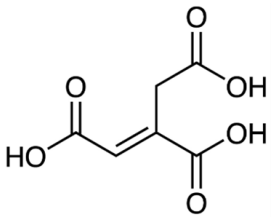

Figure 1. The structure of *trans*-aconitic acid.

Several studies have observed the change in viscosity of organic aerosols upon aging. For instance, studies on the ozonolysis of oleic acid aerosols (Hosny et al., 2016) and squalene droplets (Athanasiadis et al., 2016) indicate a significant increase in viscosity upon oxidation. SOA formed from ozonolysis of organic aerosols might also undergo additional aging, for instance photochemically, altering further the viscosity of these particles. A recent study on the photochemical aging of SOA generated from the ozonolysis of d-limonene and α-pinene shows an increase of several orders of magnitude in viscosity after UV-aging, ultimately transforming into a glassy solid state, especially at low temperatures and low relative humidities (Baboomian et al., 2022). However, to the best of our knowledge, it is not known how the aerosol properties, particularly viscosity and hygroscopicity, will change after simultaneous exposure to UV light and ozone, as simultaneously encountered in Earth's atmosphere during daytime.

In this work, we use *trans*-aconitic acid particles as surrogate for SOA to investigate how the viscosity and hygroscopicity are influenced by different degrees and different combinations of photochemical and ozone-induced aging.

2 Materials, Instrumentation, and Method

2.1 Materials

Trans-aconitic acid (AA) is a naturally occurring tricarboxylic acid that is produced by several plants and accumulates significantly in sugar cane and sweet sorghum (Bruni and Klasson, 2022). Since it is a highly oxidized molecule having carboxyl functional groups, it has low vapor pressure, and is water soluble, we use it here as a proxy system for SOA present in the atmosphere.

The UV-visible absorption spectra (Fig. 2) obtained using a UV-Visible spectrophotometer (Varian Cary 100 Bio) shows that concentrated AA solution (2.13 mol L^{-1}) absorbs

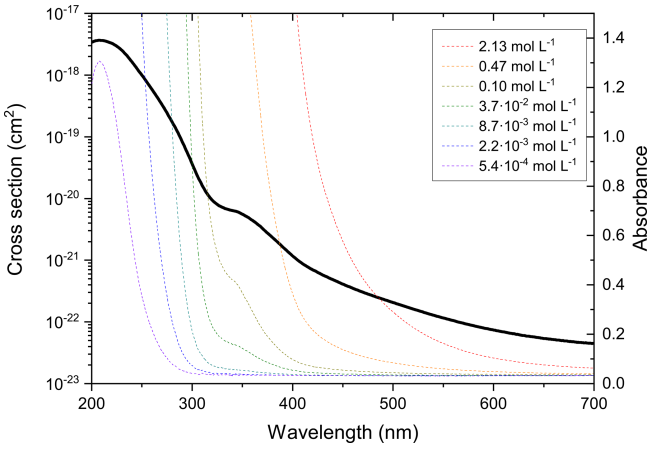

Figure 2. Absorption spectra (colored lines) and cross section (black line) of AA solution of different concentrations as a function of wavelength (absorbance values higher than 1.5 are not shown because they are above the maximum detection limit of the instrument). The cross section was calculated using Beer-Lambert's law, based on the absorbance values of the AA solutions.

even in the visible range of the solar spectrum, with significant absorbance at 375 nm. AA's absorbance at the visible to near UV wavelengths could be attributed to the conjugated structure of *trans*-aconitic acid, which makes it possible to undergo photochemical reaction at 375 nm illumination. However, it should be noted that AA (98 %, Sigma Aldrich) was used without any further purification, and it is known that the presence of even trace amounts of impurities can affect UV absorption (Saito et al., 2023). Further investigation is needed to clarify the origin of the observed absorption.

In comparison to 4-nitrocatechol, a typical brown carbon chromophore, the cross section of *trans*-aconitic acid is about 3 orders of magnitude lower between 300 and 600 nm (Cornard et al., 2005). Moreover, the presence of the double bond makes AA susceptible to ozonolysis. As a result of all these properties, AA was chosen in this study as a suitable proxy system for SOA for studying possible synergistic effects between photochemistry and ozonolysis.

2.2 Electrodynamic Balance Setup

Experiments on single, levitated, aqueous AA particles were conducted using a linear electrodynamic balance (EDB) (Fig. 3). The set-up has been described previously (Müller et al., 2022). Briefly, single aqueous AA droplets were prepared from 4 wt % AA in Milli-Q water and injected using a droplet on demand generator (HP-inkjet cartridge model 51604). The droplet was inductively charged and levitated in the EDB trap by AC and DC electric fields. 50 sccm of humidified flow from hydrocarbon free synthetic air (PanGas, 20 % O_2 in N_2) was used to keep RH in the EDB at 78 %–88 %. The radius of the particles after equilibration to RH was in the range 10–20 µm. All experiments were performed at room temperature (∼ 298 K). RH and temperature were measured using two sensors (Sensirion SHT85, Switzerland) placed at the flow entrance to the EDB as well as at the flow exit of the EDB. The sensor at the flow exit is located close to the levitated particle and it was confirmed in measurements of the deliquescence RH of NaCl particles that this sensor's RH readout is close to the RH at the location of the particle. The uncertainty in RH measurement is ±1.5 %.

Aging experiments were conducted by exposing liquid AA particles to 10 ppm ozone generated by UV photolysis of O_2 in synthetic air using an ozone generator (AOS, BMT Messtechnik, Germany). The readout of an electrochemical ozone sensor (OX-B431 on Alphasense ISB, Alphasense, UK) was used to control the ozone generator. For UV exposure, the unfocused beam of a 375 nm UV laser (Omicron LuxX-20, Germany) illuminated the particle levitated at the second segment of the EDB. Its beam profile and power lead to an irradiance at the particle location of about $(1.0 \pm 0.3)\,\mathrm{W\,cm^{-2}}$.

The O_3 exposure used in the experiments is similar to an atmospheric exposure of 100 ppb ozone for 10 d, which is a typical lifetime of atmospheric aerosols. The UV photon flux used in the experiments is a factor of 60 larger than atmospheric conditions, based on the power density of the laser irradiation and AA absorbance together with the solar irradiance integrated over the entire spectrum.

The particle was illuminated with a 532 nm diode pumped solid state laser (Thorlabs, DJ532, USA) and the scattered light was collected on CCD cameras (Raspberry Pi HQ camera, UK). The change in mass of the particle was deduced by measuring the electric force needed to balance the gravitational force of the particle. The DC voltage was adjusted by an automatic feedback loop driven by the particle image. Since in addition to the gravitational force, the DC voltage compensates for the Stokes force of the gas flow, drag force correction was applied to deduce changes in mass. The drag force was measured by setting the gas flow to 0 sccm and recording the DC voltage that needs to be applied to keep the particle levitated. Based on the difference between the DC voltage at 50 and 0 sccm, the drag force was deduced for the specific size of the particle at the time of measurement. Moreover, the size of the particle was deduced from the two-dimensional angular optical scattering (TAOS) pattern of laser-illuminated droplets. The inverse of the fringe distance along the symmetry axis of the TAOS pattern is a direct measure of the size; smaller size changes are detected by following a single maximum in the TAOS pattern. Thus, the radius of the particle was deduced from the mean distance between the fringes as long as the particle remained spherical and symmetric with regular TAOS pattern. For detecting phase transitions breaking the spherical symmetry of the particle, we use the pattern distortion parameter as introduced by Braun and Krieger (2001). More details on the radius retrieval can be found in Appendix A.

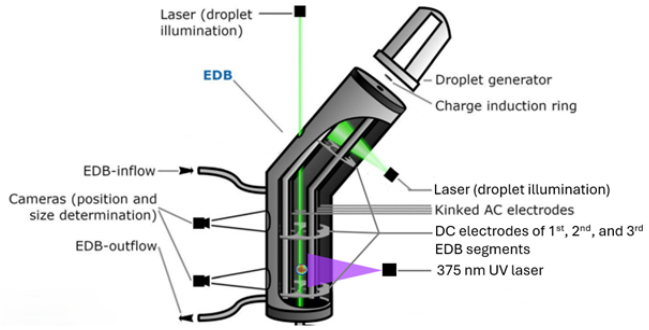

Figure 3. Schematic representation of the EDB set-up, adopted with slight modifications from Müller et al. (2022). The UV laser illuminated the particle levitated at the 2nd segment of the EDB. For simplification and better representation, the UV laser was shown in this figure in the 3rd segment of the EDB.

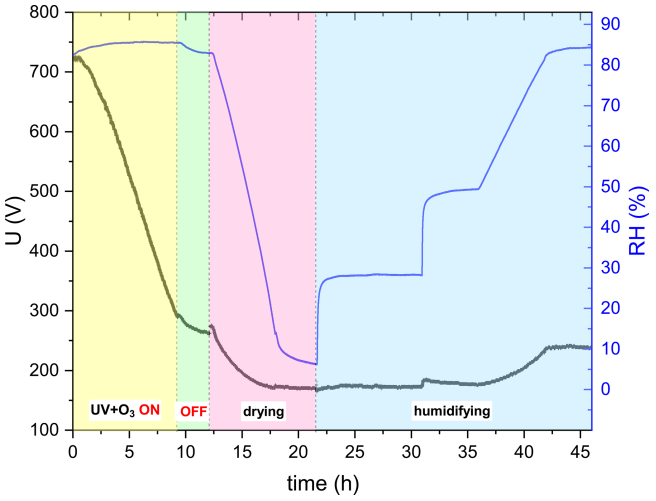

Figure 4. Overview figure showing the complete experimental procedure of AA particle exposed to UV and O_3 simultaneously until 60 % mass loss at room temperature. The black line represents the voltage needed to keep the particle levitated in the EDB (corrected for drag force), which is proportional to the mass of the particle. The blue line represents the RH data. The yellow section corresponds to switching on UV laser and O_3, the green section corresponds to turning off UV and O_3, the pink section corresponds to drying, and the blue section corresponds to humidifying.

2.3 Overview of the experimental procedure

Figure 4 shows an example of the experimental procedure to obtain hygroscopicity as well as viscosity for a combined ozonolysis and photochemical aging experiment. Initially, an aqueous AA particle is injected and levitated in the EDB. After RH is equilibrated at $\sim 83\,\%$, 375 nm UV laser and 10 ppm O_3 are switched on ($t = 0$). The change in mass is monitored and size measurements are done in parallel. The reaction is carried out at approximately constant RH, and UV illumination and O_3 are switched off after the particle loses 60 % of its initial mass. Since slight fluctuations in RH and temperature occur after switching off O_3, the particle is kept in the dark until RH, and therefore the mass and size of the particle are almost constant. Kinetics of the reaction will be discussed in Sect. 3.2. Afterwards, RH inside the EDB is decreased slowly at a rate of $0.2\,\%\,\mathrm{min}^{-1}$ from $\sim 83\,\%$ to $\sim 6\,\%$ and then kept constant for 3.5 h to ensure sufficient drying. From this drying part of the experiment, hygroscopicity is deduced, as will be explained in more detail in Sect. 2.4. Finally, RH is increased in two steps rapidly, first from 6.3 % to 28.2 %, then from 28.2 % to 49.4 %, and finally raised back from 49.4 % to 84.4 % slowly. While the flow change is indeed step-like, the response in RH is approximately exponential. The first step in humidity was used to derive condensed phase water diffusivity, as will be discussed in more detail in Sect. 2.5.

2.4 Hygroscopicity measurement

Hygroscopicity and water diffusivity measurements were done on aged particles after they lost about 20 %, 40 %, 50 %, 60 % and 80 % of their mass. For hygroscopicity measurements, RH was allowed to decrease slowly, at a rate of $0.2\,\%\,\mathrm{min}^{-1}$, by adjusting the ratio of dry nitrogen gas flow relative to the humidified flow while keeping the total flow constant using automatic mass flow controllers. The change in mass of the particles was monitored during drying using the automatic feedback loop, see Fig. 4.

The hygroscopic size growth factor ($G\,(\mathrm{RH})$) indicates the relative increase in size of the particles at a certain RH relative to dry conditions in response to water uptake. If $G\,(\mathrm{RH})$ is measured at different RH, a single parameter, κ, for hygroscopic size growth can be determined, assuming ideality (Petters and Kreidenweis, 2007):

$$G\,(\mathrm{RH}) = \frac{D(\mathrm{RH})}{D_0} = \left(1 + \kappa \frac{a_\mathrm{w}}{1 - a_\mathrm{w}}\right)^{1/3} \quad (1)$$

where $D(\mathrm{RH})$ is the mobility diameter of the particle at a certain RH, D_0 is the diameter of the particle at dry conditions, and a_w is the water activity, which is equal to RH at equilibrium.

Since here the mass growth factor ($g\,(\mathrm{RH})$) was measured instead of the size growth factor, κ can be determined from the mass growth factor by using Eq. (2) (Zardini et al., 2008):

$$g\,(\mathrm{RH}) = \frac{m(\mathrm{RH})}{m_0} = 1 + \left((G\,(\mathrm{RH}))^3 - 1\right) \frac{\rho_\mathrm{w}}{\rho_0} \quad (2)$$

Combining Eqs. (1) and (2) yields Eq. (3):

$$g(\mathrm{RH}) = 1 + \left(\kappa \frac{a_\mathrm{w}}{1 - a_\mathrm{w}} \frac{\rho_\mathrm{w}}{\rho_0}\right) \quad (3)$$

where $m(\mathrm{RH})$ is the mass of the particle at a certain RH, m_0 is the mass of the particle at dry conditions (measured

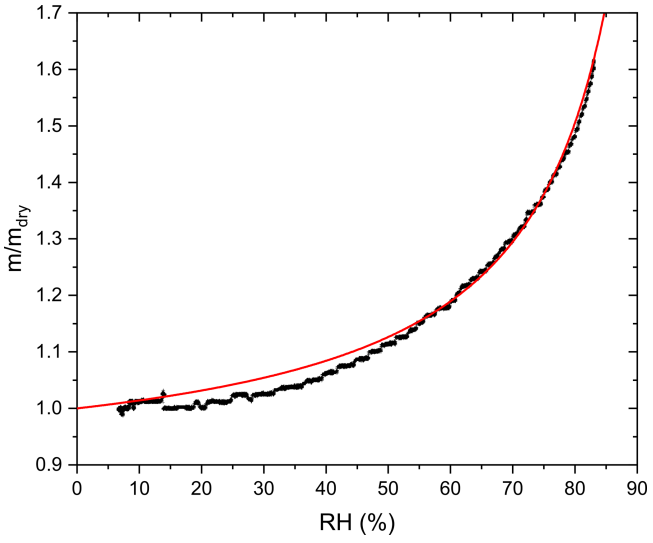

Figure 5. Mass growth factor as a function of RH for AA exposed to UV light and O_3 till 60 % mass loss (black line). The red line is the κ-parametrization fitting in the RH range 62 %–80 %, yielding a κ of 0.197.

at ∼ 6 % RH), ρ_w is the density of water, and ρ_0 is the density of the particle at dry conditions. ρ_0 for AA was determined experimentally using the conventional additivity rule and was found to be 1.56 g cm^{-3} and was assumed to remain constant after aging, see Appendix B.

Since most untreated AA effloresced at RH 59.9 %, κ-parametrization fitting according to Eq. (3) was done only in the RH range 62 %–80 % for all particles. Furthermore, fitting at higher RH provides a better estimation for κ as deviations from ideality and kinetic limitations to hygroscopic mass transfer become less important with dilution. In addition, we assume that no further chemical processing occurs once UV and O_3 are switched off. Figure 5 shows an example of the measured mass growth together with a regression of Eq. (3) to deduce κ.

2.5 Viscosity determination

Viscosity of the particles after aging was inferred indirectly by estimating the water diffusivity and then using the fractional Stokes–Einstein relation to deduce the viscosity.

For water diffusivity measurements, the aged particles were subjected to drying and were kept under low RH (below 15 %) for 4 ± 1 h, until RH stabilized around 6 %. Then, RH was increased rapidly from 6.7 ± 0.7 % to 28.6 ± 0.5 % and kept constant for 9 ± 2 h. As RH increases, water diffuses from the gas phase into the particle phase until equilibrium between water activity throughout the particle and RH of the gas phase is reached (Koop et al., 2011). The time taken to reach equilibrium depends on the viscosity of the particle, i.e. liquid droplets will reach equilibrium faster than amorphous solid or glassy particles. Thus, water diffusivity can be inferred by observing the time response in particle mass or size following a step increase in RH (Zobrist et al., 2011; Bones et al., 2012). One way of retrieving the diffusion coefficient from such data is by using a numerical model, solving the diffusion equation (Zobrist et al., 2011; O'Meara et al., 2016). Alternatively, the response of step increase in RH may be approximated by an exponential approach to the new RH setting, see data and exponential fit in Fig. 6. While a viscous liquid close to the glass transition exhibits a non-linear response leading to a non-exponential relaxation (Debenedetti and Stillinger, 2001; Rickards et al., 2015), a less viscous liquid may be reasonably well approximated by a single exponential response. Under these conditions, the hygroscopic response can be deconvoluted analytically as detailed in Appendix C. The response $y(t)$ to the hygroscopic "step" in either mass or size is then given by Eq. (4) with τ_1 being the characteristic time of the response we are searching for and τ_2 being the characteristic time of the RH step, induced by the flow change from dry to humidified.

$$y(t) = \left(1 - e^{-t/\tau_1}\right) - \frac{\tau_2}{\tau_2 - \tau_1}\left(e^{-t/t\tau_2} - e^{-t/\tau_1}\right) \quad (4)$$

Water diffusivity can then be approximately deduced from τ_1 using the following equation (Seinfeld and Pandis, 2016; Bones et al., 2012):

$$\tau_1 = \frac{r^2}{\Pi^2 D} \quad (5)$$

where $\tau_1$is the characteristic time, r is the radius of the particle, and D is the diffusion coefficient.

We show in Appendix D that this linear response approximation needs a correction to obtain D, such that it compares favorably with a full numerical model for water diffusivities in the range of 1.7×10^{-12} to 2×10^{-9} cm^2 s^{-1} and particle sizes used in our experiment.

Viscosity can then be predicted from diffusivity using Stokes–Einstein relation (Einstein, 1905):

$$D = \frac{KT}{6\Pi\eta R_{\text{diff}}} \quad (6)$$

where D is the diffusion coefficient, K is the Boltzmann constant, T is the temperature, η is the viscosity, and R_{diff} is the radius of the diffusing species. While this relation works well for large diffusing molecules in which the radius of the diffusing molecule (R_{diff}) is greater than that of the organic matrix molecule (R_{matrix}) (Chenyakin et al., 2017), it underestimates the diffusion coefficients in organic–water mixtures by several orders of magnitude for small diffusing molecules like water, where R_{diff} is smaller than R_{matrix} (Price et al., 2015; Bastelberger et al., 2017). A better approach to relate diffusivity to viscosity is to use fractional Stokes–Einstein relation where D is proportional to $1/\eta^{\xi}$, ξ being the fractional exponent, which depends on the ratio $R_{\text{diff}}/R_{\text{matrix}}$ (Evoy et al., 2020). For instance, as the ratio $R_{\text{diff}}/R_{\text{matrix}}$ decreases, ξ

decreases (Evoy et al., 2020). ξ can be expressed in terms of R_{diff}/R_{matrix} according to the following empirical equation (Evoy et al., 2020):

$$\xi = 1 - \left[0.73\exp\left(-1.79\frac{R_{diff}}{R_{matrix}}\right)\right] \quad (7)$$

The hydrodynamic radius of AA (R_{matrix}) was assumed to be the same as that of citric acid, which is structurally similar to aconitic acid, and was taken as 3.7 Å (Muller and Stokes, 1957) and for water the Van der Waals radius of 1.41 Å (Pang, 2014) was used. The hydrodynamic radius of AA was assumed to remain constant upon aging.

3 Results and Discussion

3.1 Method validation for the retrieval of diffusivity coefficient of water

To validate our approach of diffusivity coefficient retrieval, D was determined for the same experiment shown in Fig. 6 using the numerical model described in detail in Zobrist et al. (2011). The model treats the particle as consisting of up to several thousand individual shells and uses a composition and temperature dependent parametrization of the diffusion coefficient of water, simulating the growth and shrinkage of the particle resulting from water diffusion between the shells.

The model was driven by experimental RH(t) data while drying from 28 % to 6 % and then humidifying up to 28 % as well as the initial radius. For the input, several parametrizations for the water activity dependent diffusivity were tested (see Fig. 7). Parametrization for every input D was derived by linear extrapolation of diffusivity in pure water (2×10^{-5} cm^2 s^{-1}) and input D at $a_w = 0.17$ (ranging from 1×10^{-12} to 1×10^{-11} cm^2 s^{-1}), assuming that the a_w dependence of D is linear on a log scale.

As shown in Fig. 7, considerable agreement between experimental and modelled radius data is obtained when the input D was set between 3×10^{-12} and 8×10^{-12} cm^2 s^{-1}. D derived for the same particle using the linear response approximation (fitting according to Eq. 4) is 3×10^{-12} cm^2 s^{-1}. In addition, it can be clearly seen that while in the drying part the radius data retrieved from the model for the input $D = 3\times12^{-12}$ cm^2 s^{-1} does not agree well with the experimental data, it agrees quite well after the step increase in RH. This is consistent with D derived from the fitting (3×10^{-12} cm^2 s^{-1}), which is done in the same RH range, i.e. the step increase. Thus, D derived using the two different approaches agree within a factor of 2, which is chosen as the uncertainty range in our determination of D.

3.2 Kinetics: comparison between ozonolysis and photolysis

Figure 8 shows the normalized mass remaining calculated from the voltage data compensating for the gravitational force as shown in Fig. 4. The mass of an aqueous AA particle remains constant in the absence of UV irradiation at 375 nm or O_3 exposure, indicating that AA has a low vapor pressure and does not undergo any reaction in the presence of oxy-

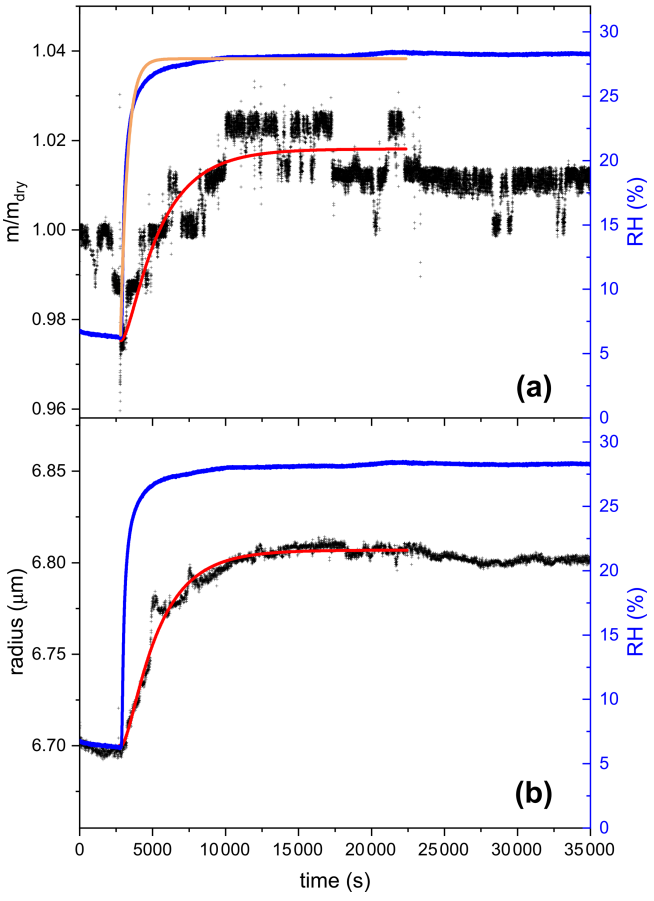

Figure 6. The response of AA to rapid changes in RH after aging with UV and O_3 until 60 % mass loss, panel **(a)** shows mass growth data and panel **(b)** size data. The blue line in both panels shows the RH data (right scale). At time $t = 2804$ s, the gas flow was switched from dry to humid with RH increasing rapidly from 6.3 % to 28.2 % and afterwards kept constant for 7.5 h. The black lines represent the response of the aged AA particle in terms of mass **(a)** and size **(b)** to the rapid increase in RH. The orange line in panel **(a)** is an exponential fit to the RH data. The red lines are the first-order kinetics fitting on the mass response **(a)** and size **(b)** response. Fitting was done only up to 22 300 s because after this time the mass and size of the particle started to decrease slightly, possibly due to volatilization of some of the remaining products or further chemical processing when RH was increased. τ_2, determined from the RH-fit, was found to be 472 s. τ_1, determined from the fitting according to Eq. (4), was found to be 2503 s for the mass response and 2312 s for the size response. Note: the step-like noise seen in the mass growth data is an artifact of the instrument, mainly due to the automatic feedback loop that adjusts the voltage to keep the particle at a fixed position, but with a finite resolution in both position and voltage. The dip in mass growth seen just before the RH step is due to sudden changes in the flow system when turning on the humid flow after drying.

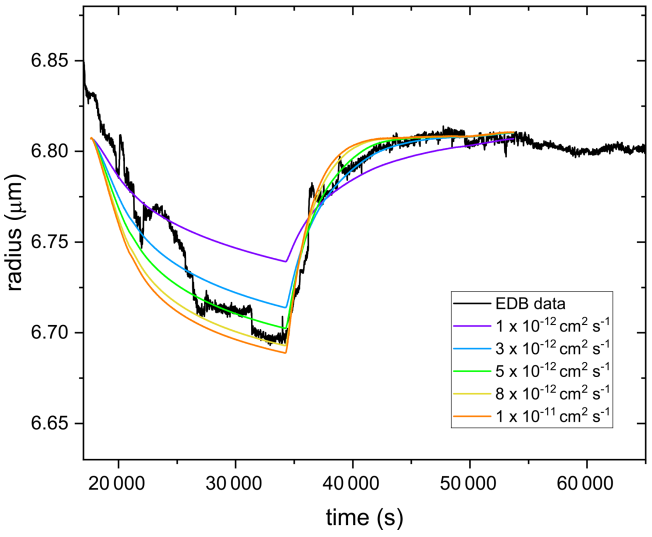

Figure 7. Radius data retrieved from the numerical model for different input $D(a_w)$ (colored lines) in the range of 1×10^{-12} cm^2 s^{-1} (violet line) to 1×10^{-11} cm^2 s^{-1} (orange line) for $D(a_w = 0.17)$ in comparison to the experimental radius data (black line) for AA particle subjected to a rapid increase in RH after aging with UV and O_3 until 60 % mass loss. Note: in the modeled data, the initial radius at RH 28 % (for all input D) is slightly lower than the equilibrium radius at the same RH after the step increase. This is because of the uncertainty in size data, as described in Appendix A.

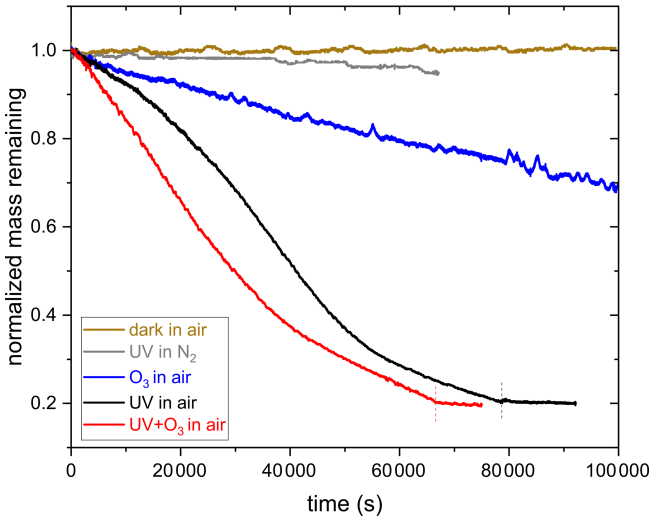

Figure 8. Comparison of the decay kinetics of an AA particle exposed to 375 nm UV irradiation in pure nitrogen and in synthetic air, 10 ppm O_3 in synthetic air, and UV+O_3 in synthetic air. Vertical dashed lines correspond to switching off UV (black) and UV+O_3 (red).

gen. In the presence of UV irradiation and/or O_3 exposure, mass loss is observed, which is evidence for the occurrence of fragmentation reactions that eventually lead to the formation of volatile products that partition from the particle phase to the gas phase. Fragmentation reactions are known to be an important pathway for organic aerosol particles undergoing photochemical reactions as well as for particles exposed to oxidants (Dou et al., 2021; Kroll et al., 2015; Sun and Smith, 2024; O'Brien and Kroll, 2019). However, as shown in Fig. 8, only slight mass loss is observed when photolysis is done under a nitrogen gas phase, highlighting the importance of oxygen in the photolysis mechanism. Acceleration in mass loss during photolysis of SOA when transitioning from nitrogen to zero air was also observed previously in a different study (Sun and Smith, 2024).

The decay kinetics of an AA particle upon reaction with ozone is linear with time, similar to a previous study (Willis and Wilson, 2022), The slow kinetics observed for ozonolysis may be due to the conjugated structure of AA, which stabilizes the C=C double bond. According to the study by Willis and Wilson (2022), most of the reactions between O_3 and AA occur in the particle bulk due to the slow reaction of AA with O_3 and AA's low surface affinity.

In contrast to ozonolysis, the shape of the photolysis decay kinetics is not linear. It is slow in the beginning, then speeds up possibly due to the formation of more photoreactive intermediates or due to the initiation of an autocatalytic process. After about 60 % mass loss, the reaction slows down again, most likely because most photoreactive species are consumed and non-absorbing products are formed (photobleaching) or because of radical recombination. We conclude that similar to the findings by O'Brien and Kroll (2019) and Sun and Smith (2024), initial photolytic mass loss cannot be extrapolated to the entire SOA mass loss and that a photo-recalcitrant fraction remains, which prevents or slows down further mass loss. In the study by Sun and Smith (2024), Suwanee River Fulvic Acid (SRFA) was used as a surrogate for brown carbon SOA. They observed that UV photolysis of an aqueous SRFA solution results in photobleaching at UV wavelengths and enhanced absorbance (photoenhancement) at visible wavelengths (Sun and Smith, 2024). For AA, UV-aging most likely results initially in photoenhancement. As the reaction proceeds, photobleaching occurs due to degradation of chromophores during fragmentation, resulting in a photo-recalcitrant fraction. These findings suggest that even a small precursor molecule, such as AA, might demonstrate a behavior similar to atmospheric brown carbon, exhibiting an alteration of optical properties upon UV-aging. However, further investigations are needed to prove that this mechanism is responsible for the observed kinetics.

Moreover, it can be inferred from Fig. 8 that the rate of decay of AA is slightly faster when photolysis is done in the presence of O_3. Since ozone is a stronger oxidant compared to oxygen, it might result in a faster mass loss, especially in the beginning of the reaction, where the oxidant is most likely the limiting factor. After the initial induction period, the rates of both reactions become comparable because of the occurrence of acceleration in the absence of O_3.

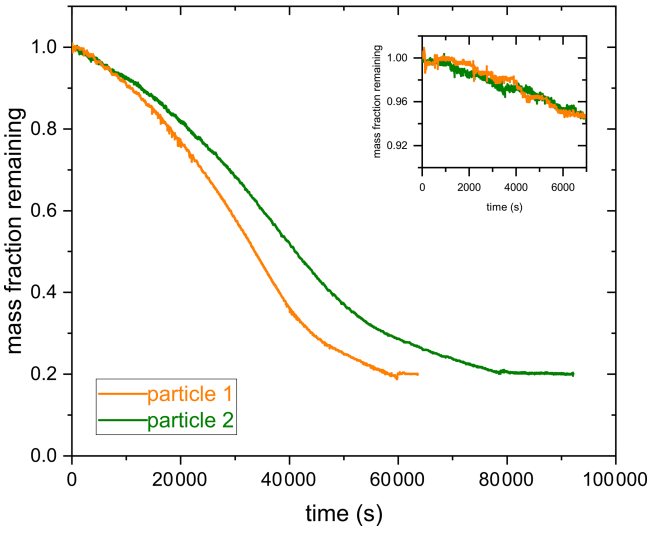

Figure 9. Comparison of the decay kinetics between two different AA particles exposed to 375 nm UV irradiation until 80 % mass loss. The inlet graph shows the first 7000 s to emphasize the overlap in the initial reaction rate between the two experiments.

Additionally, regarding the photolysis experiments, it can be inferred from Fig. 9 that the rates of reaction of two different AA particles with UV irradiation overlap in the beginning of the experiment, but acceleration in mass loss of particle 1 occurs before particle 2. For instance, after an exposure time of 40 000 s, particle 1 lost 64 % of its mass whereas particle 2 lost 48 % (see Fig. 9). This is most likely because oxygen is the rate limiting factor in the beginning of the reaction. As the reaction proceeds, the intensity of the UV irradiation becomes important, which results in different reaction rates. This might be due to slightly different particle sizes and the position of the particle relative to the laser beam, which can affect the photon flux into the particle and thus the reaction rate. For this reason, mass loss was used instead of exposure time to represent the extent of aging, as will be presented in the following sections. However, mass loss and exposure time are well correlated (see Fig. E1 in the Appendix), but mass loss was chosen to account for the differences between different particles in terms of the reaction rate, assuming that at a certain mass loss, rather than exposure time, different particles should have similar chemical composition despite having different reaction rates.

3.3 Phase separation during ozonolysis

Figure 10 shows the mean fringe distance (a) and pattern distortion parameter (b) of a 532 nm laser-illuminated AA particle upon exposure to ozone. After about an hour of O_3 exposure, the TAOS pattern of the particle becomes irregular and the pattern distortion parameter, which denotes the asymmetry in the scattering pattern (Braun and Krieger, 2001), becomes larger. This indicates that the particle is no longer homogenous and spherical and has lost its symmetry, resulting in light scattering with different intensities depending on its orientation relative to the laser beam. This behavior was observed only upon exposure to O_3 and was confirmed through five other O_3 exposure experiments, where an irregularity in the TAOS pattern was observed for all particles after an exposure time of 65 ± 8 min. On the contrary, AA particles exposed to UV illumination or UV and O_3 simultaneously remained spherical symmetric upon aging (see Fig. F1 in the Appendix). The observed heterogeneity in the particle upon ozonolysis could be due to liquid-liquid phase separation (LLPS) exhibiting partial wetting morphology. Similar behavior was observed in other studies upon ozonolysis of oleic acid particles (Hosny et al., 2016) and squalene droplets (Athanasiadis et al., 2016). However, in the case of ozonolysis of oleic acid, they observed a wide range of species: small oxidized polar molecules and large non-polar oligomers, which are immiscible and can favor LLPS. Here, we did not perform chemical characterization of the ozonolysis products, but Willis and Wilson (2022) identified products having two to seven carbon atoms with different carbon oxidation states ($\sim$ 1 to 3) in AA ozonolysis experiments. It might be possible that some of the small products with high carbon oxidation state are immiscible with the larger products with low oxidation state, which can cause phase separation. Another possibility for the observed symmetry loss in light scattering would be precipitation of *trans*-aconitic acid or one of the ozonolysis products that is insoluble in water, creating two phases: solid precipitate and dissolved liquid phase, since the particles contain significant amount of water as they are kept at relatively high RH (above 78 %), while still being lower than the deliquescence RH of AA, which is $\sim$ 96 % based on our measurements.

3.4 Phase state of AA after aging

Untreated AA particles typically effloresced at RH $\sim$ 59.9 %, but some particles did not crystallize upon drying to RH below 10 %. In contrast, AA particles aged with UV or UV and O_3 simultaneously did not crystallize upon drying. This was deduced from the TAOS pattern, which remained regular upon drying, implying that the aged particles remained liquid or amorphous solid, but not crystalline. After AA particles undergo chemical reaction, a mixture of products is produced, which makes efflorescence less likely to occur due to thermodynamic reasons (Marcolli et al., 2004).

Similar behavior in terms of suppression or inhibition of efflorescence after aging was observed previously. For instance, suppression of crystallization was observed upon ozonolysis of mixed maleic acid/ammonium sulfate particles and subsequent drying (Chan and Chan, 2012). In another study, maleic acid particles exposed to O_3 showed efflorescence at lower RH compared to unprocessed maleic acid particles, with some particles not efflorescing at any RH (Pope et al., 2010).

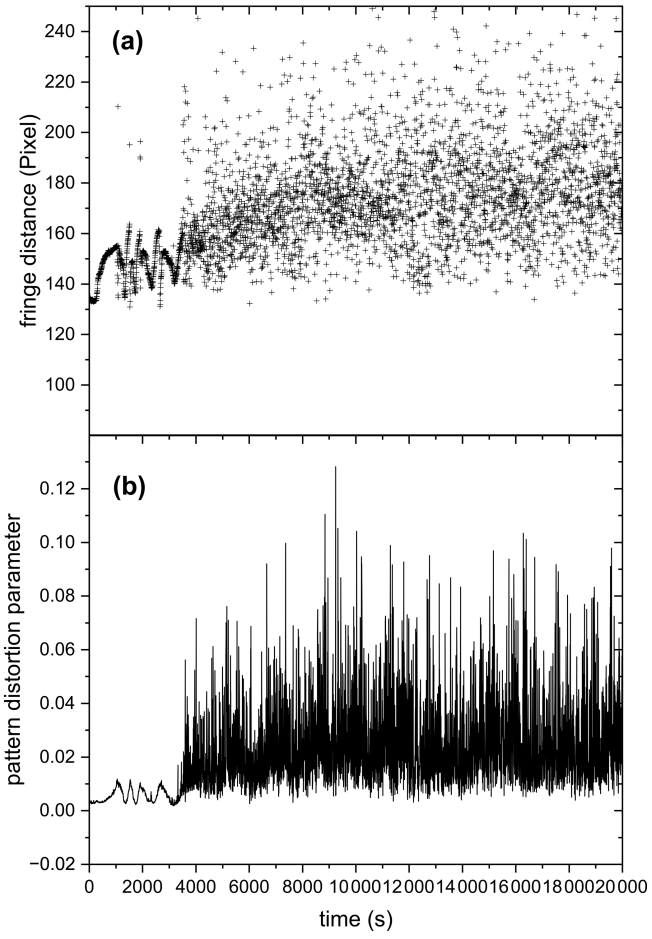

Figure 10. **(a)** Mean fringe distance and **(b)** pattern distortion parameter of 532 nm laser-illuminated AA exposed to O_3. Only the data for the first 20 000 s are plotted here to present clearly the phase transition occurring at ∼3500 s, indicated by the significant increase in fluctuations in fringe distance **(a)** and pattern distortion parameter **(b)**.

Furthermore, for AA particles aged with UV or UV and O_3 only up to 20 % or 26 % mass loss, although the particles remained spherical upon drying, the TAOS pattern became irregular after RH was increased rapidly from 6 % to 28 %, indicating crystallization of AA (see Appendix G). This could be due to restructuring the hydrogen bonding network favoring nucleation. Alternatively, if nucleation already occurred during drying, the plasticizing effect of water could lead to crystal growth after water uptake. This behavior was not observed for particles that lost more than 25 % of their mass because of the conversion of considerable amount of *trans*-aconitic acid into a mixture of products, which inhibited crystallization.

3.5 Viscosity and hygroscopicity of AA before aging

The average viscosity of untreated AA derived from our experiments at room temperature (∼ 298 K) and RH 17.7 ± 0.5 % (midpoint of the step in RH 6 %–28 %) is 1.2×10^3 Pa s. Aconitic acid and citric acid are structurally similar: both are tricarboxylic acids having 6 carbon atoms. Song et al. (2016) measured the viscosity of citric acid by droplet coalescence at ambient temperature and reported as 5.1×10^3 Pa s at 18 % RH, which is within a factor of 4 of the viscosity of AA determined in this study. The slightly higher viscosity of citric acid compared to aconitic acid might be due to the additional hydroxyl group, which enhances hydrogen bonding (Rothfuss and Petters, 2017) and the lower temperature of the coalescence experiment.

Figure 11 shows the hygroscopicity results in terms of derived κ values. For reference, a selection of κ values of other organic acids and ammonium sulfate are taken from the literature. As shown in this figure, organic acids can have quite different κ values, but are significantly lower than inorganic salts. Higher κ values indicate higher hygroscopicity (Petters and Kreidenweis, 2007). Hygroscopicity of organic compounds depends on molecular structure and physicochemical properties. Organic compounds having more functional groups, such as carboxyl, carbonyl, and hydroxyl tend to be more hygroscopic (Han et al., 2022). In general, polar organic compounds having higher O : C are more hygroscopic (Han et al., 2022; Lambe et al., 2011; Duplissy et al., 2011). In addition, organic compounds that are more water soluble tend to be more hygroscopic because they would have a higher molar concentration in the saturated solution corresponding to a stronger reduction in water activity (Han et al., 2022).

Average κ of untreated AA measured in this study is 0.254 ± 0.031, which agrees within error with *cis*-aconitic acid (0.21) determined in another study (Han et al., 2022) and that predicted by AIOMFAC model (0.237) (Zuend et al., 2011; Zuend et al., 2008), but is significantly higher than that of *trans*-aconitic acid (0.172 ± 0.010) determined in another study (Rickards et al., 2013). In our study, fitting was done between RH 62 % and 80 %, which is different from the RH used in Rickards et al. (2013) (> 90 %), which could be one reason for the difference. Variations in κ for the same organic acid between different studies have been observed previously. For instance, as shown in Fig. 11, κ for citric acid determined using a humidified tandem differential mobility analyzer (HTDMA) at RH 90 % was found to be 0.18 (Han et al., 2022), while that determined using aerosol optical tweezers (AOT) at RH 66 % was found to be 0.233 ± 0.035 (Rickards et al., 2013). In the following, we focus on changes in κ with aging rather than on absolute κ values.

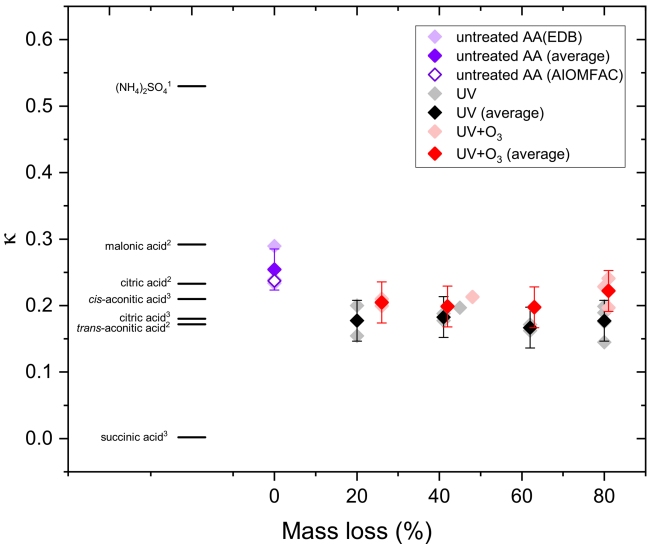

Figure 11. The hygroscopicity of AA particles before and after UV and UV+O_3 aging in comparison with $(NH_4)_2SO_4$, malonic acid, citric acid, *cis*-aconitic acid, *trans*-aconitic acid, and succinic acid data taken from the literature: (1) (Petters and Kreidenweis, 2007) (2) (Rickards et al., 2013) (3) (Han et al., 2022).

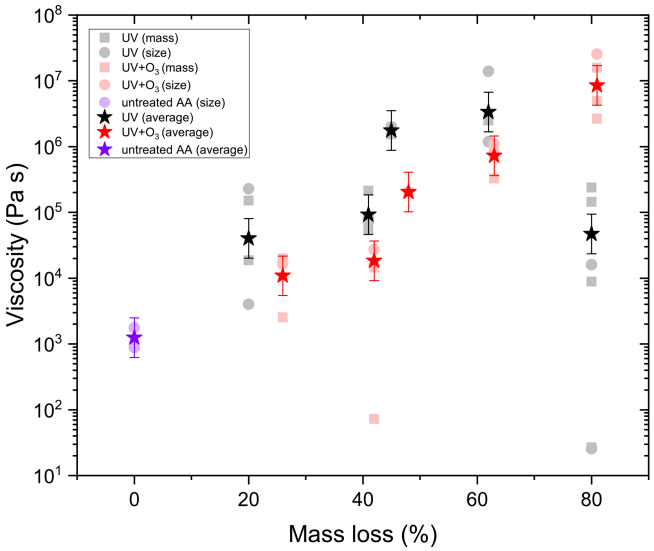

Figure 12. The viscosity of AA particles before and after UV and UV+O_3 aging from mass and/or size data.

3.6 Viscosity and hygroscopicity of AA after aging

Figure 12 shows the viscosity of untreated AA and AA aged with UV and UV and O_3 simultaneously up to 20 %, 40 %, 50 %, 60 %, and 80 % mass loss. All measurements were done at room temperature ($\sim$ 298 K) and at RH 17.7 $\pm$ 0.5 %. It should be noted that the viscosity estimates represented here are lower limit estimates. This is because we are assuming a constant fractional exponent (ξ) even though the composition of the matrix is changing significantly upon aging. Since smaller fragmentation products volatilize and are lost to the gas phase, R_{matrix} is expected to increase upon aging, thus the ratio $R_{\mathrm{diff}}/R_{\mathrm{matrix}}$ is expected to decrease. This leads to larger viscosity values when estimating from water diffusivity data using fractional Stokes–Einstein.

As shown in Fig. 12, the viscosity of AA exposed to UV and O_3 simultaneously increased with the extent of aging, with the aged AA at 80 % mass loss being almost 4 orders of magnitude higher compared to that of the untreated AA. UV exposure alone also resulted in an increase in viscosity but only up to 60 % mass loss. Surprisingly, further UV-aging (80 % mass loss) led to a reduction in viscosity. However, with UV-aging at 80 % mass loss, there is a large spread in the viscosity data, where some of the values at the lower viscosity range were beyond the limit of determination with our method (see Appendix D). Since the discrepancies in the viscosity values are mainly between size and mass measurement for the same particle, rather than being between different experiments, the uncertainty is most likely due to experimental error at 80 % mass loss, where the particle becomes small, increasing the error on both size and mass measurements. Thus, it is difficult to conclude the exact viscosity at 80 % mass loss, but it is evident that the viscosity in all cases is significantly less than the one at 60 % mass loss.

As shown in Fig. 11, average κ of aqueous AA particles decreased slightly from 0.254 $\pm$ 0.031 to 0.177 $\pm$ 0.031 upon aging with UV light till 20 % mass loss. Upon further aging, κ remained almost constant. For the AA particles aged with UV and O_3 simultaneously, less significant reduction in κ was observed. Similar to UV-aging, κ decreased from 0.254 $\pm$ 0.031 to 0.205 $\pm$ 0.031 after 25 % mass loss, but then it remained almost constant with further aging. However, this reduction is not significant, taking the uncertainty in κ into account. In addition, overall κ values for UV+O_3 aged AA are a bit higher than those of UV-aged AA, consistent with the viscosity values, which show slightly lower viscosity for UV+O_3 aged AA up to 60 % mass loss.

Currently, we do not have any information about the chemical composition of the particles after aging. However, we may draw some conclusions from the data shown in Figs. 11 and 12. Since hygroscopicity did not increase after aging, O : C is also expected to remain almost constant or decrease slightly after aging. While it is known that hygroscopicity and carbon oxidation state increase after oxidative aging (Jimenez et al., 2009; Kroll et al., 2011, 2015), no significant or small net change in O : C was observed after photolysis of SOA in other studies (Romonosky et al., 2015; O'Brien and Kroll, 2019). It should be noted that in this study, only the hygroscopicity and viscosity of the condensed phase after aging are measured, without considering the highly volatile compounds evaporating to the gas phase. It is still expected that the overall carbon oxidation state increased after aging in our study if the compounds lost to the gas phase are also considered. As gas phase oxidants are involved in the aging process

(O_2 in UV-aging and O_3 in UV+O_3 aging), it is expected that polar oxygen containing functional groups are added after oxidation. Since these groups weaken adjacent C-C bonds, fragmentation reactions will take place, leading to volatilization of smaller fragments to the gas phase. This mechanism can be indirectly inferred from Fig. 8, where initially an induction period appears, followed by rapid mass loss. However, it is expected that the most highly oxidized carbon will exist mainly in the gas phase (Kroll et al., 2011). Therefore, although the small, fragmented products are expected to have higher oxidation state, they are also expected to be volatile, thus the oxidation state of the particle can decrease slightly after these fragments evaporate (O'Brien and Kroll, 2019; Hildebrandt Ruiz et al., 2015). However, we cannot prove that O : C remained constant or decreased slightly, since we did not determine the chemical composition of the products. Note that if O : C increased after aging, but if the average molecular weight increased as well, the hygroscopicity may still decrease.

Viscosity increase upon SOA aging was observed previously in the UV-aging of d-limonene and α-pinene SOA (Baboomian et al., 2022). Mass spectrometric analysis indicated that the increase in d-limonene SOA viscosity was most likely due to changes in the chemical properties because an average increase in molecular weight, elemental O : C ratio, number of carbon atoms per molecule, and double bond equivalent was observed (Baboomian et al., 2022). However, in contrast to our study, photolysis of SOA was done at low RH. Water content of the particle during photolysis can play an important role in the mechanism of formation of products and thus in the viscosity of the final products. For instance, when photolysis of SOA was performed in aqueous solution instead of low RH, reduction in carbon number was observed, which was attributed to the degradation of dimers and trimers (Romonosky et al., 2015). Another study comparing condensed-phase SOA photolysis at low RH and aqueous photolysis found that the signal intensity obtained by mass spectrometry in the larger m/z range remained similar before and after exposure, while lower m/z range was higher after aqueous photolysis, but lower after condensed-phase photolysis (Sun and Smith, 2024). They attributed this difference to the evaporation of the volatile products from the condensed phase, but retention of these species in the aqueous solution. Direct comparison of our study to these studies is difficult, since in our case condensed-phase photolysis was done at higher RH. However, since mass loss was observed and the viscosity increased after UV-aging, it can be inferred that the smaller volatile fragments evaporated, leaving relatively larger non-volatile products in the particle.

One possible explanation for the observed viscosity enhancement after aging is the formation of oligomers from product fragments. Oligomers, due to their high molecular weight, could contribute to increased viscosity. However, the formation of oligomers might be hindered under the experimental conditions, as the reactions occur at moderately high RH, and the presence of water typically slows down oligomerization (Kalberer et al., 2004). It is important to note, though, that the particles are more concentrated in water at these RH levels (even at 85 %) compared to typical aqueous-phase chemistry, which may facilitate oligomer formation. Additionally, oligomerization could have occurred during the drying process just before viscosity measurements were taken.

Alternatively, the increase in viscosity could be attributed to changes in the hydrogen bonding network. The intermolecular hydrogen bonding between the products might be enhanced compared to untreated AA, leading to a higher viscosity. Further UV-aging could degrade some of these products or the oligomers, potentially altering the hydrogen bonding interactions and causing a decrease in viscosity upon continued aging.

The continuous increase in viscosity upon aging with UV and O_3 simultaneously until 80 % mass loss suggests that the aging mechanism and the products formed are different in the presence of oxidants like O_3. The presence of O_3 might favor the formation of oligomers, therefore increasing the viscosity of the particles further with longer exposure.

4 Conclusions

In this study, the viscosity and hygroscopicity of aqueous *trans*-aconitic acid particles were determined after exposure to 375 nm UV irradiation or UV irradiation and O_3. Photolysis and ozonolysis resulted in significant mass loss because of fragmentation reactions followed by volatilization and displayed different reaction kinetics. Ozonolysis alone disrupted the light scattering symmetry of the particle, indicating a phase transition. Aging with UV or UV and O_3 resulted in the inhibition of efflorescence upon drying. The viscosity of the particles increased by almost 4 orders of magnitude upon aging with UV and O_3 simultaneously. UV-aging also resulted in an increase in viscosity but only up to 60 % mass loss. Further UV-aging resulted in a reduction in viscosity. Hygroscopicity of the particles decreased slightly after exposure to UV laser up to 20 % mass loss and then stayed constant with further aging. A similar trend, though less significant, was observed for combined UV and O_3 aging.

To check the relevance of our study to atmospheric conditions, we estimated the characteristic mixing times within the particles after aging. The increase in viscosity upon aging implies for particles with a radius of 100 nm (typical of accumulation mode SOA particles) a characteristic mixing time of 4 h compared to 4 s for the unexposed particles under dry boundary layer conditions, at RH $\sim$ 17 % and 298 K. For colder temperatures in the free troposphere, the mixing times could be still longer even at higher relative humidity. As a result, higher viscosity and mixing times are expected to extend particle lifetime and promote longer-range transport by

reducing susceptibility to washout and further chemical processing.

Therefore, the changes in viscosity, hygroscopicity, phase state, volatility, and mixing times observed in this study provide further evidence on how aging can directly alter the physicochemical properties of aerosol particles, with indirect consequences on climate and human health. Our results show that the presence of gas phase oxidants like ozone, in addition to UV light, results in viscosity enhancement, an effect seen previously in the UV-aging of SOA. This viscosity enhancement is most likely due to the formation of oligomers of high molecular weight. However, from the shape of reaction kinetics, hygroscopicity, and viscosity results, we conclude that the mechanism of aging is different in the presence of gas phase oxidants compared to photochemical aging without gas phase oxidants. Thus, further studies on simultaneous aging are needed to determine whether the effects observed in this study can be extended to other systems. To understand better the mechanism behind the differences that we observe, we plan to study in the future the chemical composition of the products during aging using mass spectrometry.

Appendix A: Size retrieval from two-dimensional angular optical scattering (TAOS) pattern

The EDB configuration and geometrical constraints allow us to measure the TAOS pattern within about 5° half apex angle around 100° scattering. Figure A1 shows four TAOS-patterns observed in our experiments.

Comparing Fig. A1d with the other panels of Fig. A1 illustrate that the regular TAOS pattern is distorted once the spherical symmetry of a particle is lost. In comparison to Fig. A1b, the average fringe distance for both orthogonal fringe patterns in Fig. A1c has increased, indicating shrinkage during aging. Quantitative analysis of these types of patterns, i.e. size retrieval, has been discussed extensively in the literature (Davis and Periasamy, 1985; Steiner et al., 1999; Jakubczyk et al., 2013; Davies, 2019). A fast, simple method for sizing a spherical symmetric particle is based on scattered light angular frequency determination (Steiner et al., 1999), which requires a calibration of the TAOS pattern in terms of scattering angle. We follow the suggestion by Davies (2019) and measure the evaporation rate of a pure compound for calibration, here PEG-4 for which the vapor pressure is well established (Krieger et al., 2018).

Sizing by measuring the characteristic angular frequency works best for scattering angles smaller than 60°. However, our scattering angle is 100° and our apex angle is quite small due to spatial restriction in our setup. This limits its applicability to small size changes, as the uncertainty in sizing using the characteristic angular frequency is of the order of ±1 µm for our scattering geometry and typical particle size. Therefore, for measuring small size changes, we apply a method based on spectral shift of Mie-resonance spectra (Zardini et al., 2006) to angular shift of a peak position in the TAOS pattern. Compare this approach with a related method based on tabulated peak positions suggested by Davies (2019). Figure A2 shows data taken for an evaporating PEG-4 particle at constant temperature. Panel (a) shows that the radius scales almost linearly over a wide size range with the total peak position shift in the TAOS pattern. On closer inspection (see panel (b) of Fig. A2), the relationship is irregular on small scales but allows the reliable detection of size changes of about ±40 nm. In our application, we are focusing on characteristic time scales of small size changes due to rapid changes in relative humidity: there, the irregularity between size and peak position shift for small size changes influences the determination of characteristic time only slightly (see Fig. 6 in main text.)

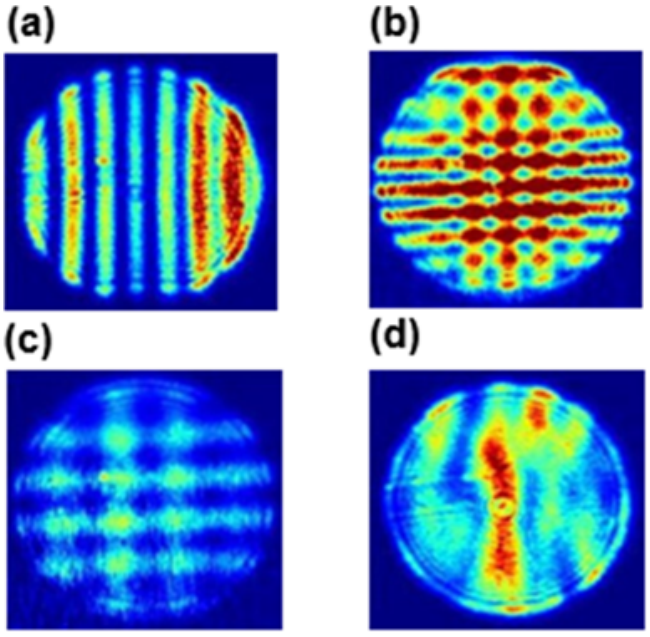

Figure A1. **(a)** TAOS pattern of a spherical symmetric *trans*-aconitic acid particle upon illumination with polarized 532 nm laser, fringe intensity is rainbow color coded in arbitrary units. **(b)** Pattern of a particle upon illumination by both the polarized 532 nm laser and the orthogonally polarized 375 nm laser. **(c)** same as **(b)** but after photochemical aging. **(d)** TAOS pattern for 532 nm illumination only after phase transition induced by ozonolysis.

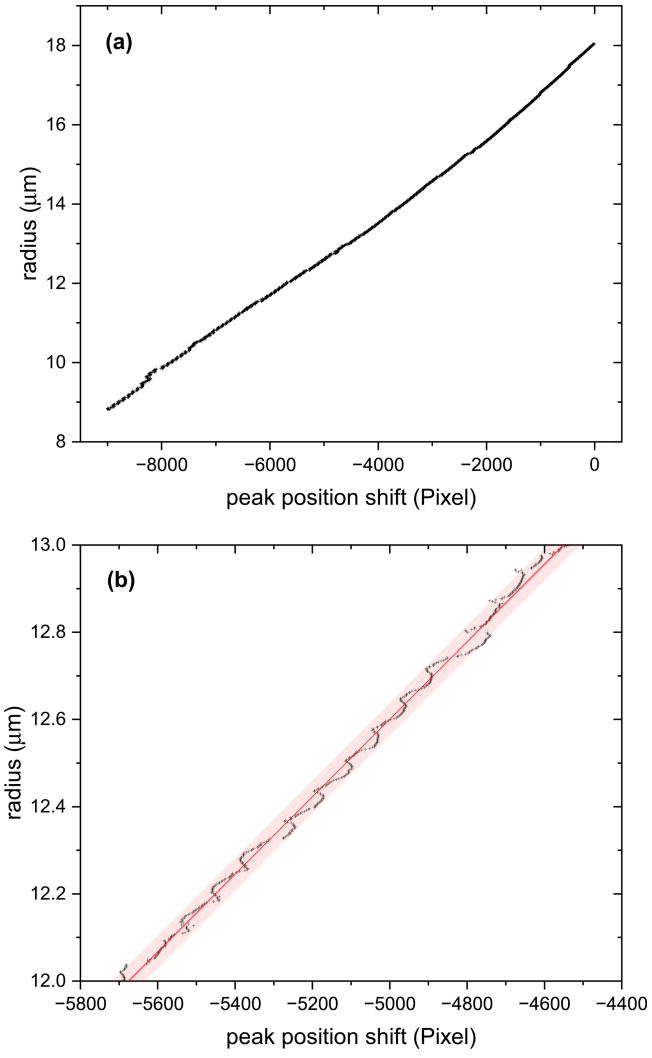

Figure A2. **(a)** Size data of an evaporation experiment (PEG-4 at 24 °C) versus peak position shift. Evaporation rate was calculated from known data of vapor pressure (Krieger et al., 2018) and radius was determined through comparison of measured characteristic angular frequency with evaporation rate. **(b)** Zoom into the data of **(a)** showing that radius can be measured with a sensitivity of about ±40 nm when measuring the peak position shift. Note however, that the relationship between peak position shift and size is not strictly linear, but irregular within a size change of approximately 40 nm.

Appendix B: Density determination of aqueous AA

To determine the density of aqueous AA under dry conditions (ρ_0), the density of AA at mass fraction $w_s = 0.286$ was measured using a pycnometer. Assuming the conventional additivity rule holds (Lienhard et al., 2012; Steimer et al., 2015):

$$\rho(w_s) = \left(\frac{1 - w_s}{\rho_w} + \frac{w_s}{\rho_0}\right) \tag{B1}$$

where $\rho(w_s)$ is the density of solute at mass fraction w_s, ρ_w is the density of water, we retrieve ρ_0, the density of aqueous AA solute at dry conditions, i.e. the subcooled melt density. Based on the known density of water and our measured density at $w_s = 0.286$, $\rho_0 = 1.56\,\mathrm{g\,cm^{-3}}$.

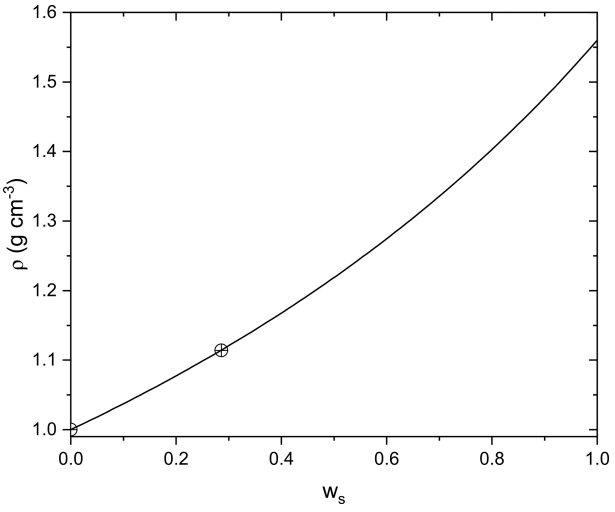

Figure B1. Density (ρ) vs. mass fraction (w_s) parametrization for aqueous AA according to Eq. (B1).

Appendix C: Deconvolution of linear response to an exponential "step" in relative humidity, derivation of Eq. (4)

Let's assume the dynamic system is a linear time-invariant one, with the response of the system to a step input (Heaviside function, $H(t)$) is given by:

$$y(t) = 1 - e^{-k_1 t} \tag{C1}$$

Now, instead of a step input, $H(t)$, the input function is given by:

$$\mathrm{RH}(t) = 1 - e^{-k_2 t} \tag{C2}$$

In our experiment, we obtain k_2 by analyzing the data RH(t), with k_2 being the rate constant of the RH-step. We want to determine the system's response $y(t)$ to the input RH(t). Very generally, the system's response is given by the convolution integral:

$$y(t) = \int_0^t \mathrm{RH}(\tau)\, h(t - \tau)\, \mathrm{d}\tau \tag{C3}$$

where the impulse response $h(t)$ is the derivative of the system to a step response $H(t)$:

$$h(t) = k_1 e^{-k_1 t},\ t > 0 \tag{C4}$$

For the step response, $H(t)$, the radius or mass evolution is related to the impulse response by:

$$y(t) = \int_0^t h(\tau)\,\mathrm{d}\tau \tag{C5}$$

Therefore, substituting the RH input function and the impulse response function by $h(t-\tau) = k_1 e^{-k_1(t-\tau)}$, we get:

$$y(t) = \int_0^t \left(1 - e^{-k_2(\tau)}\right) k_1 e^{-k_1(t-\tau)}\,\mathrm{d}\tau \tag{C6}$$

Expanding the integral:

$$y(t) = k_1 e^{-k_1 t} \int_0^t \left(1 - e^{-k_2\tau}\right) e^{k_1\tau}\,\mathrm{d}\tau \tag{C7}$$

Solving the integral leads to the final expression for $y(t)$:

$$y(t) = \left(1 - e^{-k_1 t}\right) - \frac{k_1}{k_1 - k_2}\left(e^{-k_2 t} - e^{-k_1 t}\right) \tag{C8}$$

Replacing the rate constants with their inverse, i.e. the characteristic time constants $\tau_1 = 1/k_1$ and $\tau_2 = 1/k_2$, yields Eq. (4):

$$y(t) = \left(1 - e^{-t/\tau_1}\right) - \frac{\tau_2}{\tau_2 - \tau_1}\left(e^{-t/\tau_2} - e^{-t/\tau_1}\right) \tag{C9}$$

Appendix D: Comparing the linear response approximation of Appendix C to a numerical model solving the diffusion equation

As noted in the main text, the linear response approximation for water uptake kinetics is expected to diverge from the full solution of Fick's second law when water diffusivity becomes sufficiently slow. Here, we compare the size change resulting from water uptake under an ideal exponential "step"-like change in RH, using a numerical model based on the Euler forward method to solve the diffusion equation (Zobrist et al., 2011), with the linear approximation described in Appendix C.

Since we use the same flow changes in all our experiments and the particle sizes in the experiments vary only over a rather small size range, we can restrict the comparison to an idealized RH(t) pathway taken from our experimental observations as well as choosing a particular initial radius. Figure D1 shows the RH(t) pathway chosen as a blue line, the size response predicted by the numerical model as a black line and a linear regression of Eq. (4) to the size predicted by the numerical model as a red line. For simplicity, we assume as input for the numerical model that the dependence of water diffusivity on water activity follows an exponential dependence for water activities with the water diffusivity for pure water fixed to 2×10^{-5} cm^2 s^{-1}. At 40 % RH, an initial radius of 6.969 µm is set and it is assumed that at this starting RH before drying the particle is internally mixed in water content. For the simulation of Fig. D1, we set the water diffusivity D ($a_w = 0.17$) to 2×10^{-10} cm^2 s^{-1}. As evident from Fig. D1 for these parameters, the linear approximation seems to mirror the predictions of the numerical model very well.

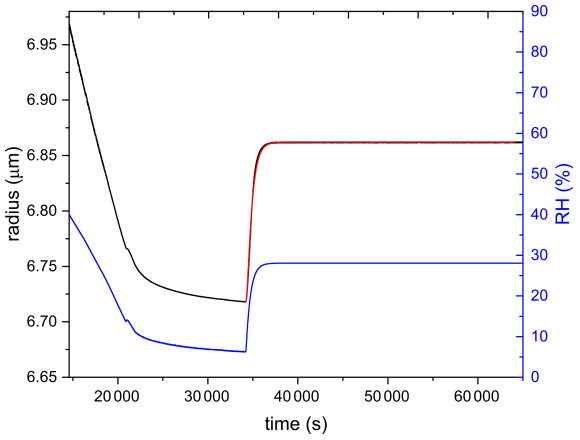

Figure D1. The blue line represents the RH data. The black line represents the radius data obtained from the numerical model for an input D of 2×10^{-10} cm^2 s^{-1}. The red line is the first-order kinetics fitting according to Eq. (4) on the size response data after increasing RH rapidly.

Following this approach, we test the linear response for the range of D ($a_w = 0.17$) between 5×10^{-13} to 2×10^{-7} cm^2 s^{-1}. Some of the results are shown in Fig. D2. It becomes clear that our experiments are not sensitive to D (at $a_w = 0.17$) $> 2 \times 10^{-9}$ cm^2 s^{-1}, simply because our experimental setup yields a rather slow response in RH(t) upon a step change in gas mass flows (We cannot increase the total flow much beyond 50 sccm to allow mass measurements). For this reason, the second step increase in RH (from 28 % to 49 %), shown in Fig. 4 in the main text, was not evaluated. Figure D2 shows in addition the expected deviation from linear response with low water diffusivities (panels e and f).

However, we can correct for the differences between numerical model and linear approximation for a limited range of water diffusivities as shown in Fig. D3. There, we compare the characteristic time constant, τ_1, obtained from the linear regression to Eq. (4) to the input parameters of the numerical model represented as characteristic time according to Eq. (5). Perfect agreement between both is indicated as the dashed line. The limited range of characteristic response times for which the linear approximation works is clearly visible from Fig. D3. It allows us to deduce an empirical correction factor which we apply for characteristic response times measured in our experiments ranging from 20 to about 27 000 s. Fortunately, this is approximately the time range we do observe in our experiments for untreated AA and the most viscous aged particles.

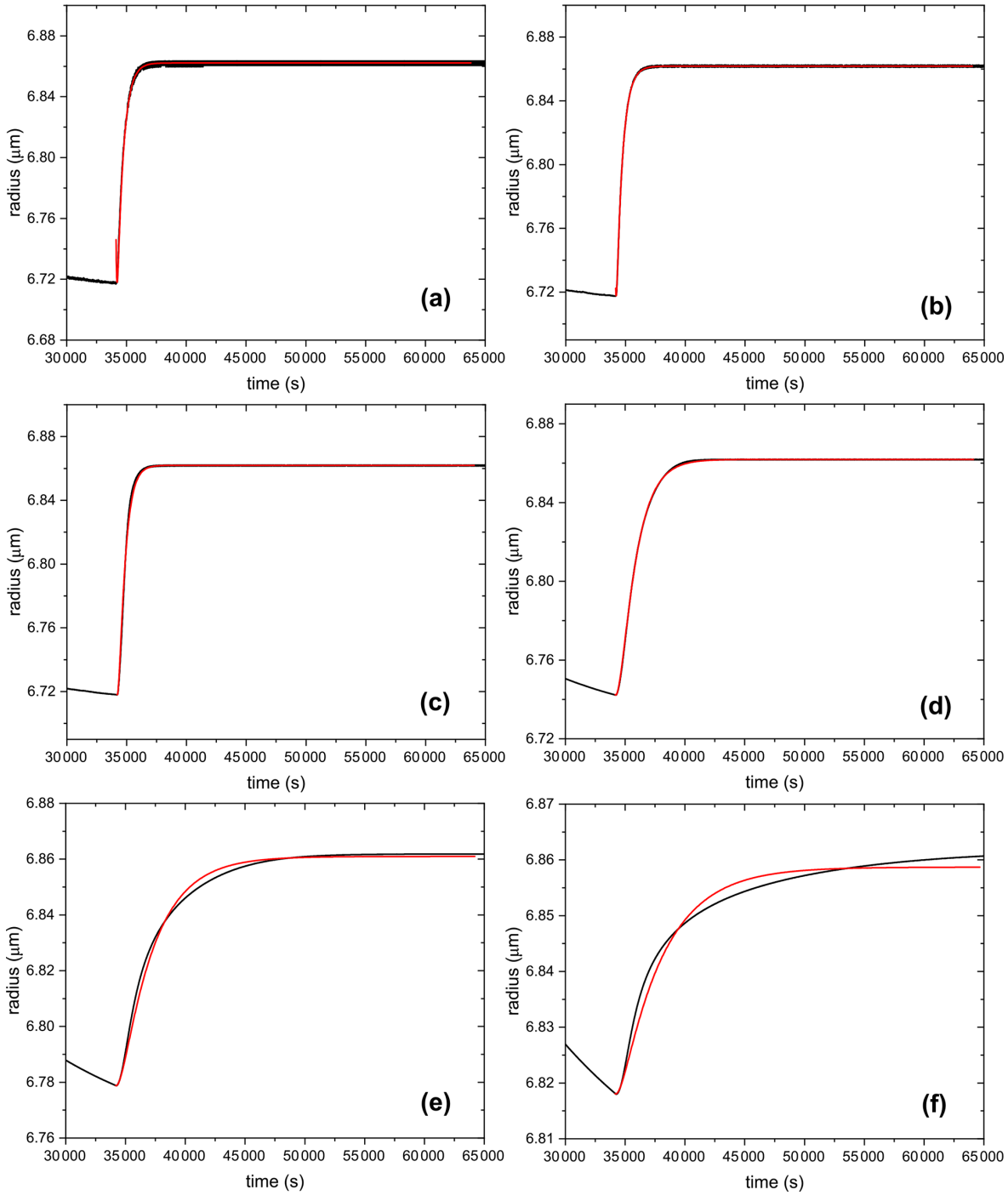

Figure D2. The black line represents the size data obtained from the numerical model for an input D (at $a_w = 0.17$) of **(a)** 2×10^{-8} cm^2 s^{-1}, **(b)** 2×10^{-9} cm^2 s^{-1}, **(c)** 2×10^{-10} cm^2 s^{-1}, **(d)** 9×10^{-12} cm^2 s^{-1}, **(e)** 2×10^{-12} cm^2 s^{-1}, and **(f)** 5×10^{-13} cm^2 s^{-1}. The red line shows the linear response approximation regression curve.

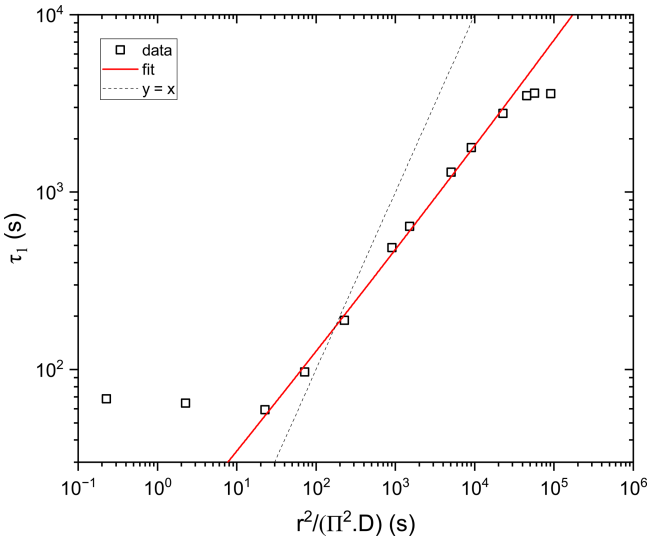

Figure D3. Output τ_1 data determined using the exponential function vs. input $r^2/(\Pi^2 D)$ data determined using the numerical model. The red line represents the fit on the output vs. input data. The dashed line shows $\tau_1 = \frac{r^2}{\Pi^2.D}$.

Appendix E: Correlation between mass loss and exposure time

Figure E1 shows that as mass loss increases, exposure time also increases for both UV and UV+O_3 exposure. This means that mass loss and exposure time are well correlated. Thus, % mass loss can be used to represent the extent of aging.

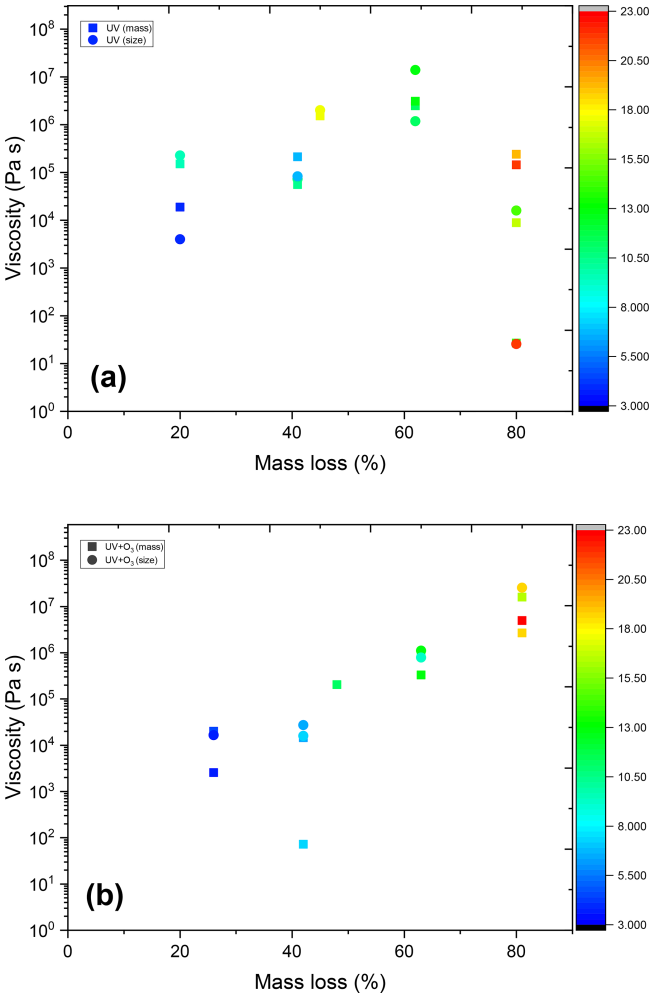

Figure E1. Viscosity of AA particles as a function of mass loss color-coded according to the exposure time (h) for **(a)** UV-exposure experiments and **(b)** UV+O_3.

Appendix F: Mean fringe distance of AA particle exposed to UV up to 80 % mass loss

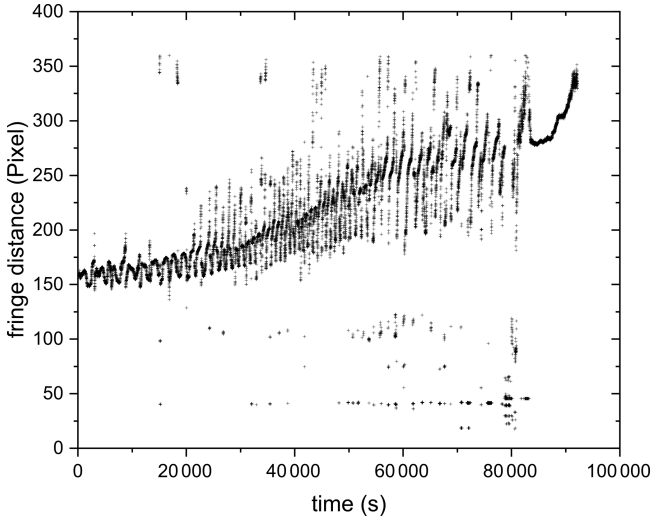

Figure F1. Mean fringe distance of AA particle exposed to UV up to 80 % mass loss. While the fringe distance oscillates with size change, TAOS pattern is clearly visible throughout the entire experiment, indicating the absence of phase transition.

Appendix G: Mean fringe distance and pattern distortion parameter of AA particle exposed to UV and O_3 up to 26 % mass loss upon humidifying

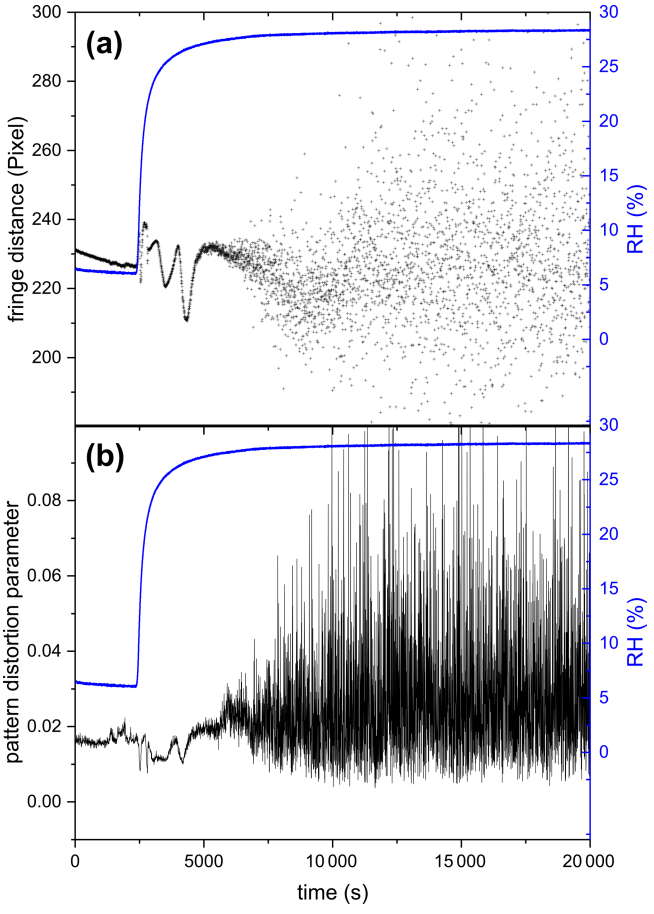

Figure G1. **(a)** Mean fringe distance and **(b)** pattern distortion parameter of AA particle exposed to UV and O_3 up to 26 % mass loss upon increasing RH from 6.0 % to 28.4 %. Significant increase in fluctuations in fringe distance **(a)** and pattern distortion parameter **(b)** are observed at 6000 s, indicating the efflorescence of AA.

Data availability. All data of the figures are available online at https://doi.org/10.3929/ethz-c-000788184 (Antossian et al., 2025).

Author contributions. Funding was acquired by UKK. Experiments were conceptualized by UKK and CA and carried out by CA. The data were analyzed by CA and UKK. The manuscript was written by CA and revised by UKK and MM.

Competing interests. The contact author has declared that none of the authors has any competing interests.

Disclaimer. Publisher's note: Copernicus Publications remains neutral with regard to jurisdictional claims made in the text, published maps, institutional affiliations, or any other geographical representation in this paper. The authors bear the ultimate responsibility for providing appropriate place names. Views expressed in the text are those of the authors and do not necessarily reflect the views of the publisher.

Acknowledgements. The authors would like to thank Colette Heald for providing helpful feedback on the manuscript. The authors would like to acknowledge Kristopher McNeill and Oleksandr Yushckenko for their assistance in the absorbance measurements.

Financial support. This research has been supported by the Eidgenössische Technische Hochschule Zürich (grant no. 23-1 ETH-020).

Review statement. This paper was edited by Sergey A. Nizkorodov and reviewed by three anonymous referees.

References

Antossian, C., Müller, M., and Krieger, U. K.: Photochemical and ozone-induced aging significantly alter the viscosity of aqueous trans-aconitic acid aerosol particles (Data collection), ETH Research Collection [data set], https://doi.org/10.3929/ethz-c-000788184, 2025.

Athanasiadis, A., Fitzgerald, C., Davidson, N. M., Giorio, C., Botchway, S. W., Ward, A. D., Kalberer, M., Pope, F. D., and Kuimova, M. K.: Dynamic viscosity mapping of the oxidation of squalene aerosol particles, Phys. Chem. Chem. Phys., 18, 30385–30393, https://doi.org/10.1039/c6cp05674a, 2016.

Baboomian, V. J., Crescenzo, G., Huang, Y. Z., Mahrt, F., Shiraiwa, M., Bertram, A. K., and Nizkorodov, S. A.: Sunlight can convert atmospheric aerosols into a glassy solid state and modify their environmental impacts, Proc. Natl. Acad. Sci. USA, 119, https://doi.org/10.1073/pnas.2208121119, 2022.

Bastelberger, S., Krieger, U. K., Luo, B., and Peter, T.: Diffusivity measurements of volatile organics in levitated viscous aerosol particles, Atmos. Chem. Phys., 17, 8453–8471, https://doi.org/10.5194/acp-17-8453-2017, 2017.

Bones, D. L., Reid, J. P., Lienhard, D. M., and Krieger, U. K.: Comparing the mechanism of water condensation and evaporation in glassy aerosol, Proc. Natl. Acad. Sci. USA, 109, 11613–11618, https://doi.org/10.1073/pnas.1200691109, 2012.

Braun, C. and Krieger, U. K.: Two dimensional angular light scattering in aqueous NaCl single aerosol particles during deliquescence and efflorescence, Opt. Express, 8, 314–321, https://doi.org/10.1364/oe.8.000314, 2001.

Bruni, G. O. and Klasson, K. T.: Aconitic Acid Recovery from Renewable Feedstock and Review of Chemical and Biological Applications, Foods, 11, 18, https://doi.org/10.3390/foods11040573, 2022.

Chan, L. P. and Chan, C. K.: Roles of the Phase State and Water Content in Ozonolysis of Internal Mixtures of Maleic Acid and Ammonium Sulfate Particles, Aerosol Sci. Technol., 46, 781–793, https://doi.org/10.1080/02786826.2012.665514, 2012.

Chan, M. N., Kreidenweis, S. M., and Chan, C. K.: Measurements of the hygroscopic and deliquescence properties of organic compounds of different solubilities in water and their relationship with cloud condensation nuclei activities, Environ. Sci. Technol., 42, 3602–3608, https://doi.org/10.1021/es7023252, 2008.

Chenyakin, Y., Ullmann, D. A., Evoy, E., Renbaum-Wolff, L., Kamal, S., and Bertram, A. K.: Diffusion coefficients of organic molecules in sucrose-water solutions and comparison with Stokes-Einstein predictions, Atmos. Chem. Phys., 17, 2423-2435, https://doi.org/10.5194/acp-17-2423-2017, 2017.

Cornard, J. P., Rasmiwetti, and Merlin, J. C.: Molecular structure and spectroscopic properties of 4-nitrocatechol at different pH: UV-visible, Raman, DFT and TD-DFT calculations, Chem. Phys., 309, 239–249, https://doi.org/10.1016/j.chemphys.2004.09.020, 2005.

Davies, J. F.: Mass, charge, and radius of droplets in a linear quadrupole electrodynamic balance, Aerosol Sci. Technol., 53, 309–320, https://doi.org/10.1080/02786826.2018.1559921, 2019.

Davis, E. J. and Periasamy, R.: Light-scattering and aerodynamic size measurements for homogeneous and inhomogeneous microspheres, Langmuir, 1, 373–379, https://doi.org/10.1021/la00063a020, 1985.

Debenedetti, P. G. and Stillinger, F. H.: Supercooled liquids and the glass transition, Nature, 410, 259–267, https://doi.org/10.1038/35065704, 2001.

Dockery, D. W. and Pope, C. A.: Acute respiratory effects of particulate air-pollution, Annu. Rev. Public Health, 15, 107–132, https://doi.org/10.1146/annurev.pu.15.050194.000543, 1994.

Dou, J., Alpert, P. A., Corral Arroyo, P., Luo, B., Schneider, F., Xto, J., Huthwelker, T., Borca, C. N., Henzler, K. D., Raabe, J., Watts, B., Herrmann, H., Peter, T., Ammann, M., and Krieger, U. K.: Photochemical degradation of iron(III) citrate/citric acid aerosol quantified with the combination of three complementary experimental techniques and a kinetic process model, Atmos. Chem. Phys., 21, 315–338, https://doi.org/10.5194/acp-21-315-2021, 2021.

Duplissy, J., DeCarlo, P. F., Dommen, J., Alfarra, M. R., Metzger, A., Barmpadimos, I., Prevot, A. S. H., Weingartner, E., Tritscher, T., Gysel, M., Aiken, A. C., Jimenez, J. L., Canagaratna, M. R., Worsnop, D. R., Collins, D. R., Tomlinson, J., and Bal-

tensperger, U.: Relating hygroscopicity and composition of organic aerosol particulate matter, Atmos. Chem. Phys., 11, 1155–1165, https://doi.org/10.5194/acp-11-1155-2011, 2011.

Einstein, A.: Über die von der molekularkinetischen Theorie der Wärme geforderte Bewegung von in ruhenden Flüssigkeiten suspendierten Teilchen, Ann. Phys., 17, 549–560, 1905.

Evoy, E., Kamal, S., Patey, G. N., Martin, S. T., and Bertram, A. K.: Unified Description of Diffusion Coefficients from Small to Large Molecules in Organic-Water Mixtures, J. Phys. Chem. A, 124, 2301–2308, https://doi.org/10.1021/acs.jpca.9b11271, 2020.

Gou, Y. F., Xie, M. J., and Chen, J.: The phase state and viscosity of organic aerosol and related impacts on atmospheric physicochemical processes: A review, Atmos. Environ., 343, 17, https://doi.org/10.1016/j.atmosenv.2024.120985, 2025.

Han, S., Hong, J., Luo, Q., Xu, H., Tan, H., Wang, Q., Tao, J., Zhou, Y., Peng, L., He, Y., Shi, J., Ma, N., Cheng, Y., and Su, H.: Hygroscopicity of organic compounds as a function of organic functionality, water solubility, molecular weight, and oxidation level, Atmos. Chem. Phys., 22, 3985–4004, https://doi.org/10.5194/acp-22-3985-2022, 2022.

Hildebrandt Ruiz, L., Paciga, A. L., Cerully, K. M., Nenes, A., Donahue, N. M., and Pandis, S. N.: Formation and aging of secondary organic aerosol from toluene: changes in chemical composition, volatility, and hygroscopicity, Atmos. Chem. Phys., 15, 8301–8313, https://doi.org/10.5194/acp-15-8301-2015, 2015.

Hosny, N. A., Fitzgerald, C., Vysniauskas, A., Athanasiadis, A., Berkemeier, T., Uygur, N., Pöschl, U., Shiraiwa, M., Kalberer, M., Pope, F. D., and Kuimova, M. K.: Direct imaging of changes in aerosol particle viscosity upon hydration and chemical aging, Chem. Sci., 7, 1357–1367, https://doi.org/10.1039/c5sc02959g, 2016.

Jakubczyk, D., Derkachov, G., Kolwas, M., and Kolwas, K.: Combining weighting and scatterometry: Application to a levitated droplet of suspension, J. Quant. Spectrosc. Ra. Trans., 126, 99–104, https://doi.org/10.1016/j.jqsrt.2012.11.010, 2013.

Jimenez, J. L., Canagaratna, M. R., Donahue, N. M., Prevot, A. S. H., Zhang, Q., Kroll, J. H., DeCarlo, P. F., Allan, J. D., Coe, H., Ng, N. L., Aiken, A. C., Docherty, K. S., Ulbrich, I. M., Grieshop, A. P., Robinson, A. L., Duplissy, J., Smith, J. D., Wilson, K. R., Lanz, V. A., Hueglin, C., Sun, Y. L., Tian, J., Laaksonen, A., Raatikainen, T., Rautiainen, J., Vaattovaara, P., Ehn, M., Kulmala, M., Tomlinson, J. M., Collins, D. R., Cubison, M. J., Dunlea, E. J., Huffman, J. A., Onasch, T. B., Alfarra, M. R., Williams, P. I., Bower, K., Kondo, Y., Schneider, J., Drewnick, F., Borrmann, S., Weimer, S., Demerjian, K., Salcedo, D., Cottrell, L., Griffin, R., Takami, A., Miyoshi, T., Hatakeyama, S., Shimono, A., Sun, J. Y., Zhang, Y. M., Dzepina, K., Kimmel, J. R., Sueper, D., Jayne, J. T., Herndon, S. C., Trimborn, A. M., Williams, L. R., Wood, E. C., Middlebrook, A. M., Kolb, C. E., Baltensperger, U., and Worsnop, D. R.: Evolution of Organic Aerosols in the Atmosphere, Science, 326, 1525–1529, https://doi.org/10.1126/science.1180353, 2009.

Kalberer, M., Paulsen, D., Sax, M., Steinbacher, M., Dommen, J., Prevot, A. S. H., Fisseha, R., Weingartner, E., Frankevich, V., Zenobi, R., and Baltensperger, U.: Identification of polymers as major components of atmospheric organic aerosols, Science, 303, 1659–1662, https://doi.org/10.1126/science.1092185, 2004.

Kanakidou, M., Seinfeld, J. H., Pandis, S. N., Barnes, I., Dentener, F. J., Facchini, M. C., Van Dingenen, R., Ervens, B., Nenes, A., Nielsen, C. J., Swietlicki, E., Putaud, J. P., Balkanski, Y., Fuzzi, S., Horth, J., Moortgat, G. K., Winterhalter, R., Myhre, C. E. L., Tsigaridis, K., Vignati, E., Stephanou, E. G., and Wilson, J.: Organic aerosol and global climate modelling: a review, Atmos. Chem. Phys., 5, 1053–1123, https://doi.org/10.5194/acp-5-1053-2005, 2005.

Koop, T., Bookhold, J., Shiraiwa, M., and Pöschl, U.: Glass transition and phase state of organic compounds: dependency on molecular properties and implications for secondary organic aerosols in the atmosphere, Phys. Chem. Chem. Phys., 13, 19238–19255, https://doi.org/10.1039/c1cp22617g, 2011.

Krieger, U. K., Siegrist, F., Marcolli, C., Emanuelsson, E. U., Gøbel, F. M., Bilde, M., Marsh, A., Reid, J. P., Huisman, A. J., Riipinen, I., Hyttinen, N., Myllys, N., Kurtén, T., Bannan, T., Percival, C. J., and Topping, D.: A reference data set for validating vapor pressure measurement techniques: homologous series of polyethylene glycols, Atmos. Meas. Tech., 11, 49–63, https://doi.org/10.5194/amt-11-49-2018, 2018.

Kroll, J. H. and Seinfeld, J. H.: Chemistry of secondary organic aerosol: Formation and evolution of low-volatility organics in the atmosphere, Atmos. Environ., 42, 3593–3624, https://doi.org/10.1016/j.atmosenv.2008.01.003, 2008.

Kroll, J. H., Lim, C. Y., Kessler, S. H., and Wilson, K. R.: Heterogeneous Oxidation of Atmospheric Organic Aerosol: Kinetics of Changes to the Amount and Oxidation State of Particle-Phase Organic Carbon, J. Phys. Chem. A, 119, 10767–10783, https://doi.org/10.1021/acs.jpca.5b06946, 2015.

Kroll, J. H., Donahue, N. M., Jimenez, J. L., Kessler, S. H., Canagaratna, M. R., Wilson, K. R., Altieri, K. E., Mazzoleni, L. R., Wozniak, A. S., Bluhm, H., Mysak, E. R., Smith, J. D., Kolb, C. E., and Worsnop, D. R.: Carbon oxidation state as a metric for describing the chemistry of atmospheric organic aerosol, Nat. Chem., 3, 133–139, https://doi.org/10.1038/nchem.948, 2011.

Kuwata, M. and Martin, S. T.: Phase of atmospheric secondary organic material affects its reactivity, Proc. Natl. Acad. Sci. USA, 109, 17354–17359, https://doi.org/10.1073/pnas.1209071109, 2012.

Lambe, A. T., Onasch, T. B., Massoli, P., Croasdale, D. R., Wright, J. P., Ahern, A. T., Williams, L. R., Worsnop, D. R., Brune, W. H., and Davidovits, P.: Laboratory studies of the chemical composition and cloud condensation nuclei (CCN) activity of secondary organic aerosol (SOA) and oxidized primary organic aerosol (OPOA), Atmos. Chem. Phys., 11, 8913–8928, https://doi.org/10.5194/acp-11-8913-2011, 2011.

Lienhard, D. M., Bones, D. L., Zuend, A., Krieger, U. K., Reid, J. P., and Peter, T.: Measurements of Thermodynamic and Optical Properties of Selected Aqueous Organic and Organic-Inorganic Mixtures of Atmospheric Relevance, J. Phys. Chem. A, 116, 9954–9968, https://doi.org/10.1021/jp3055872, 2012.

Marcolli, C. and Krieger, U. K.: Relevance of Particle Morphology for Atmospheric Aerosol Processing, Trends Chem., 2, 1–3, https://doi.org/10.1016/j.trechm.2019.11.008, 2020.

Marcolli, C., Luo, B. P., Peter, Th., and Wienhold, F. G.: Internal mixing of the organic aerosol by gas phase diffusion of semivolatile organic compounds, Atmos. Chem. Phys., 4, 2593–2599, https://doi.org/10.5194/acp-4-2593-2004, 2004.

Mu, Q., Shiraiwa, M., Octaviani, M., Ma, N., Ding, A. J., Su, H., Lammel, G., Pöschl, U., and Cheng, Y. F.: Temperature effect on phase state and reactivity controls atmospheric multiphase chemistry and transport of PAHs, Sci. Adv., 4, 8, https://doi.org/10.1126/sciadv.aap7314, 2018.

Muller, G. T. A. and Stokes, R. H.: the mobility of the undissociated citric acid molecule in aqueous solution, transactions of the Faraday Society, 53, 642–645, https://doi.org/10.1039/tf9575300642, 1957.

Müller, M., Mishra, A., Berkemeier, T., Hausammann, E., Peter, T., and Krieger, U. K.: Electrodynamic balance-mass spectrometry reveals impact of oxidant concentration on product composition in the ozonolysis of oleic acid, Phys. Chem. Chem. Phys., 24, 27086–27104, https://doi.org/10.1039/d2cp03289a, 2022.

Murray, B. J., Wilson, T. W., Dobbie, S., Cui, Z. Q., Al-Jumur, S., Möhler, O., Schnaiter, M., Wagner, R., Benz, S., Niemand, M., Saathoff, H., Ebert, V., Wagner, S., and Kärcher, B.: Heterogeneous nucleation of ice particles on glassy aerosols under cirrus conditions, Nat. Geosci., 3, 233–237, https://doi.org/10.1038/ngeo817, 2010.

Nel, A.: Air pollution-related illness: Effects of particles, Science, 308, 804–806, https://doi.org/10.1126/science.1108752, 2005.

O'Brien, R. E. and Kroll, J. H.: Photolytic Aging of Secondary Organic Aerosol: Evidence for a Substantial Photo-Recalcitrant Fraction, J. Phys. Chem. Lett., 10, 4003-4009, https://doi.org/10.1021/acs.jpclett.9b01417, 2019.

O'Meara, S., Topping, D. O., and McFiggans, G.: The rate of equilibration of viscous aerosol particles, Atmos. Chem. Phys., 16, 5299–5313, https://doi.org/10.5194/acp-16-5299-2016, 2016.

Pang, X. F.: Water: Molecular Structure and Properties, World Scientific Publishing Co. Pte. Ltd., https://doi.org/10.1142/8669, 2014.

Pankow, J. F.: An absorption-model of the gas aerosol partitioning involved in the formation of secondary organic aerosol, Atmos. Environ., 28, 189–193, https://doi.org/10.1016/1352-2310(94)90094-9, 1994.

Petters, M. D. and Kreidenweis, S. M.: A single parameter representation of hygroscopic growth and cloud condensation nucleus activity, Atmos. Chem. Phys., 7, 1961–1971, https://doi.org/10.5194/acp-7-1961-2007, 2007.

Pope, F. D., Gallimore, P. J., Fuller, S. J., Cox, R. A., and Kalberer, M.: Ozonolysis of Maleic Acid Aerosols: Effect upon Aerosol Hygroscopicity, Phase and Mass, Environ. Sci. Technol., 44, 6656–6660, https://doi.org/10.1021/es1008278, 2010.

Pöschl, U. and Shiraiwa, M.: Multiphase Chemistry at the Atmosphere-Biosphere Interface Influencing Climate and Public Health in the Anthropocene, Chem. Rev., 115, 4440–4475, https://doi.org/10.1021/cr500487s, 2015.

Price, H. C., Mattsson, J., Zhang, Y., Bertram, A. K., Davies, J. F., Grayson, J. W., Martin, S. T., O'Sullivan, D., Reid, J. P., Rickards, A. M. J., and Murray, B. J.: Water diffusion in atmospherically relevant α-pinene secondary organic material, Chem. Sci., 6, 4876–4883, https://doi.org/10.1039/c5sc00685f, 2015.

Rickards, A. M. J., Miles, R. E. H., Davies, J. F., Marshall, F. H., and Reid, J. P.: Measurements of the Sensitivity of Aerosol Hygroscopicity and the κ Parameter to the O/C Ratio, J. Phys. Chem. A, 117, 14120-14131, https://doi.org/10.1021/jp407991n, 2013.

Rickards, A. M. J., Song, Y. C., Miles, R. E. H., Preston, T. C., and Reid, J. P.: Variabilities and uncertainties in characterising water transport kinetics in glassy and ultraviscous aerosol, Phys. Chem. Chem. Phys., 17, 10059–10073, https://doi.org/10.1039/c4cp05383d, 2015.

Romonosky, D. E., Laskin, A., Laskin, J., and Nizkorodov, S. A.: High-Resolution Mass Spectrometry and Molecular Characterization of Aqueous Photochemistry Products of Common Types of Secondary Organic Aerosols, J. Phys. Chem. A, 119, 2594–2606, https://doi.org/10.1021/jp509476r, 2015.

Rothfuss, N. E. and Petters, M. D.: Influence of Functional Groups on the Viscosity of Organic Aerosol, Environ. Sci. Technol., 51, 271–279, https://doi.org/10.1021/acs.est.6b04478, 2017.

Saito, S., Numadate, N., Teraoka, H., Enami, S., Kobayashi, H., and Hama, T.: Impurity contribution to ultraviolet absorption of saturated fatty acids, Sci. Adv., 9, 7, https://doi.org/10.1126/sciadv.adj6438, 2023.

Seinfeld, J. H. and Pandis, S. N.: Atmospheric chemistry and physics: from air pollution to climate change, 3rd Edn., John Wiley & Sons, Inc., ISBN: 9781119221166, 2016.

Shiraiwa, M., Ammann, M., Koop, T., and Pöschl, U.: Gas uptake and chemical aging of semisolid organic aerosol particles, Proc. Natl. Acad. Sci. USA, 108, 11003–11008, https://doi.org/10.1073/pnas.1103045108, 2011.

Shrivastava, M., Lou, S., Zelenyuk, A., Easter, R. C., Corley, R. A., Thrall, B. D., Rasch, P. J., Fast, J. D., Simonich, S. L. M., Shen, H. Z., and Tao, S.: Global long-range transport and lung cancer risk from polycyclic aromatic hydrocarbons shielded by coatings of organic aerosol, Proc. Natl. Acad. Sci. USA, 114, 1246–1251, https://doi.org/10.1073/pnas.1618475114, 2017.

Song, Y. C., Haddrell, A. E., Bzdek, B. R., Reid, J. P., Barman, T., Topping, D. O., Percival, C., and Cai, C.: Measurements and Predictions of Binary Component Aerosol Particle Viscosity, J. Phys. Chem. A, 120, 8123–8137, https://doi.org/10.1021/acs.jpca.6b07835, 2016.

Steimer, S. S., Krieger, U. K., Te, Y.-F., Lienhard, D. M., Huisman, A. J., Luo, B. P., Ammann, M., and Peter, T.: Electrodynamic balance measurements of thermodynamic, kinetic, and optical aerosol properties inaccessible to bulk methods, Atmos. Meas. Tech., 8, 2397–2408, https://doi.org/10.5194/amt-8-2397-2015, 2015.

Steiner, B., Berge, B., Gausmann, R., Rohmann, J., and Rühl, E.: Fast in situ sizing technique for single levitated liquid aerosols, Appl. Optics, 38, 1523–1529, https://doi.org/10.1364/ao.38.001523, 1999.

Sun, M. R. and Smith, G. D.: Photolytic Mass Loss of Humic Substances Measured with a Quartz Crystal Microbalance, ACS Earth Space Chem., 8, 1623–1633, https://doi.org/10.1021/acsearthspacechem.4c00134, 2024.

Willis, M. D. and Wilson, K. R.: Coupled Interfacial and Bulk Kinetics Govern the Timescales of Multiphase Ozonolysis Reactions, J. Phys. Chem. A, 126, 4991–5010, https://doi.org/10.1021/acs.jpca.2c03059, 2022.

Wolf, M. J., Zhang, Y., Zawadowicz, M. A., Goodell, M., Froyd, K., Freney, E., Sellegri, K., Rösch, M., Cui, T. Q., Winter, M., Lacher, L., Axisa, D., DeMott, P. J., Levin, E. J. T., Gute, E., Abbatt, J., Koss, A., Kroll, J. H., Surratt, J. D., and Cziczo, D. J.: A biogenic secondary organic aerosol source of cirrus ice nucleating particles, Nat. Commun., 11, 9, https://doi.org/10.1038/s41467-020-18424-6, 2020.

Zardini, A. A., Krieger, U. K., and Marcolli, C.: White light Mie resonance spectroscopy used to measure very low vapor pressures of substances in aqueous solution aerosol particles, Opt. Express, 14, 6951–6962, https://doi.org/10.1364/oe.14.006951, 2006.

Zardini, A. A., Sjogren, S., Marcolli, C., Krieger, U. K., Gysel, M., Weingartner, E., Baltensperger, U., and Peter, T.: A combined particle trap/HTDMA hygroscopicity study of mixed inorganic/organic aerosol particles, Atmos. Chem. Phys., 8, 5589–5601, https://doi.org/10.5194/acp-8-5589-2008, 2008.

Zaveri, R. A., Easter, R. C., Shilling, J. E., and Seinfeld, J. H.: Modeling kinetic partitioning of secondary organic aerosol and size distribution dynamics: representing effects of volatility, phase state, and particle-phase reaction, Atmos. Chem. Phys., 14, 5153–5181, https://doi.org/10.5194/acp-14-5153-2014, 2014.

Zelenyuk, A., Imre, D., Beránek, J., Abramson, E., Wilson, J., and Shrivastava, M.: Synergy between Secondary Organic Aerosols and Long-Range Transport of Polycyclic Aromatic Hydrocarbons, Environ. Sci. Technol., 46, 12459–12466, https://doi.org/10.1021/es302743z, 2012.

Zhang, Q., Jimenez, J. L., Canagaratna, M. R., Allan, J. D., Coe, H., Ulbrich, I., Alfarra, M. R., Takami, A., Middlebrook, A. M., Sun, Y. L., Dzepina, K., Dunlea, E., Docherty, K., DeCarlo, P. F., Salcedo, D., Onasch, T., Jayne, J. T., Miyoshi, T., Shimono, A., Hatakeyama, S., Takegawa, N., Kondo, Y., Schneider, J., Drewnick, F., Borrmann, S., Weimer, S., Demerjian, K., Williams, P., Bower, K., Bahreini, R., Cottrell, L., Griffin, R. J., Rautiainen, J., Sun, J. Y., Zhang, Y. M., and Worsnop, D. R.: Ubiquity and dominance of oxygenated species in organic aerosols in anthropogenically-influenced Northern Hemisphere midlatitudes, Geophys. Res. Lett., 34, https://doi.org/10.1029/2007gl029979, 2007.

Zobrist, B., Soonsin, V., Luo, B. P., Krieger, U. K., Marcolli, C., Peter, T., and Koop, T.: Ultra-slow water diffusion in aqueous sucrose glasses, Phys. Chem. Chem. Phys., 13, 3514–3526, https://doi.org/10.1039/c0cp01273d, 2011.

Zuend, A., Marcolli, C., Luo, B. P., and Peter, T.: A thermodynamic model of mixed organic-inorganic aerosols to predict activity coefficients, Atmos. Chem. Phys., 8, 4559–4593, https://doi.org/10.5194/acp-8-4559-2008, 2008.

Zuend, A., Marcolli, C., Booth, A. M., Lienhard, D. M., Soonsin, V., Krieger, U. K., Topping, D. O., McFiggans, G., Peter, T., and Seinfeld, J. H.: New and extended parameterization of the thermodynamic model AIOMFAC: calculation of activity coefficients for organic-inorganic mixtures containing carboxyl, hydroxyl, carbonyl, ether, ester, alkenyl, alkyl, and aromatic functional groups, Atmos. Chem. Phys., 11, 9155–9206, https://doi.org/10.5194/acp-11-9155-2011, 2011.